

# Field measurements demonstrate distinct initiation and cessation thresholds governing aeolian sediment transport flux

Raleigh L. Martin\*, Department of Atmospheric and Oceanic Sciences, University of California, Los Angeles, CA 90095

Jasper F. Kok, Department of Atmospheric and Oceanic Sciences, University of California, Los Angeles, CA 90095

## Key Points

1. We provide the first field-based evidence for separate fluid and impact thresholds in aeolian saltation
2. Saltation occurrence is mediated by both thresholds, but fluid (impact) threshold dominates during infrequent (near-continuous) transport
3. Both thresholds are important for high-frequency saltation prediction, but long-term aeolian fluxes are governed mostly by impact threshold

\*raleighm@atmos.ucla.edu

## Abstract

Wind-blown sand and dust models depend sensitively on the threshold wind stress. However, laboratory and numerical experiments suggest the coexistence of distinct “fluid” and “impact” thresholds for the initiation and cessation of aeolian saltation, respectively. Because aeolian transport models typically use a single threshold, existence of dual thresholds complicates the prediction of wind-driven transport. Here, we derive the first field-based estimates of distinct fluid and impact thresholds from high-frequency saltation measurements at three field sites. Our measurements show that, when saltation is mostly inactive, its instantaneous occurrence is governed primarily by wind exceedance of the fluid threshold. As saltation activity increases, so too does the relative importance of the impact threshold, until it dominates under near-continuous transport conditions. Although both thresholds are thus important for high-frequency saltation prediction, we find that the time-averaged saltation flux is primarily governed by impact threshold.

## 1. Introduction

Determining the threshold wind shear stress for the occurrence of wind-driven (“aeolian”) sand transport has been a central challenge for studies of planetary, coastal, and desert aeolian processes [e.g., *Bagnold*, 1941; *Iversen and White*, 1982; *Shao and Lu*, 2000]. In desert and semi-arid environments, the aeolian saltation threshold regulates the frequency of topsoil erosion and mineral dust emission [e.g., *Rice et al.*, 1999]. Where sand dunes and ripples are present, the saltation threshold governs the frequency of migration of these bedforms [e.g., *Fryberger et al.*, 1979]. Recent aeolian transport studies indicate that sand flux scales linearly [e.g., *Ho et al.*, 2011; *Martin and Kok*, 2017] with wind stress in excess of the saltation threshold, so shifts in the presumed threshold value can substantially change predictions of the total sand saltation flux and associated dust emissions [e.g., *Sherman et al.*, 2013; *Kok et al.*, 2014; *Webb et al.*, 2016].

Uncertainty in threshold is therefore a major issue for studies relating aeolian transport observations to atmospheric conditions on Earth [e.g., *Lindhorst and Betzler, 2016*], Mars [e.g., *Bridges et al., 2012; Ayoub et al., 2014*], and other planetary surfaces [e.g., *Lorenz and Zimbelman, 2014*].

Despite the central importance of the saltation threshold in predicting sand and dust fluxes, there remains a lack of agreement over the best way to model or even measure this threshold [*Barchyn and Hugenholtz, 2011*]. Predictive equations for saltation (and the resulting dust emission) usually include a single threshold value [*Barchyn et al., 2014b*], traditionally the “fluid threshold” shear stress  $\tau_{ft}$  for initiating saltation transport solely by aerodynamic forces [*Bagnold, 1941; Iversen and White, 1982; Marticorena and Bergametti, 1995*]. However, theory and measurements suggest the presence of a separate, lower “impact threshold” shear stress  $\tau_{it}$  required to sustain saltation through saltator impacts with the soil bed. This impact threshold has been hypothesized to equal the rate of momentum dissipation at the surface [*Owen, 1964*], which is controversial [*Kok et al., 2012*], but for which there is now limited experimental support [*Walter et al., 2014*].

Based on the role of the impact threshold in the steady-state saltation momentum balance, most recent saltation models use impact threshold alone as the zero-intercept value for the saltation flux law [*Ungar and Haff, 1987; Creysse et al., 2009; Martin and Kok, 2017*]. However, recent studies have argued for the need to simulate the path-dependence of saltation flux responses to turbulent wind fluctuations around both impact and fluid thresholds [*Kok, 2010a, 2010b*]. The ratio of impact and fluid thresholds governing this hysteresis depends primarily on the particle-fluid density ratio, which determines the relative contributions of particle impacts and direct fluid lifting to particle entrainment [*Kok, 2010b; Pähzt and Durán, 2017*]. On Earth, the experimentally [*Bagnold, 1937*] and numerically [*Kok, 2010b*] predicted ratio of impact and fluid threshold shear velocities  $u_{*it}/u_{*ft}$  is approximately 0.82, whereas  $u_{*it}/u_{*ft}$  is predicted to be as low as 0.1 on Mars [*Kok, 2010a*].

Though numerical and experimental studies predict fluid and impact thresholds, field studies have not yet confirmed the existence of these two separate thresholds, let alone determined which should be used for modeling sand and dust flux. Field-based determinations of fluid and impact threshold have been hindered by the generally poor correlation between time series of wind speed and saltation flux at short time scales [e.g., *Wiggs et al., 2004b; Davidson-Arnott et al., 2005; Davidson-Arnott and Bauer, 2009*], due to spatial separation between saltation and wind measurements [*Baas, 2008*], variability in surface grain configurations [*Nickling, 1988; Li et al., 2008*], and fluctuations in the turbulent winds driving saltation [*Carneiro et al., 2015*].

Here, we use extensive high-frequency field measurements of aeolian transport at three field sites to determine which threshold(s) should be used in models for sand and dust flux. In the following sections, we develop a “dual threshold hypothesis” for how fluid and impact thresholds determine the effective threshold governing the frequency of saltation activity (Section 2), describe methods for calculating these saltation activities and effective thresholds from field measurements (Section 3), use these calculations to test the dual threshold hypothesis and derive field-based estimates of separate fluid and impact thresholds (Section 4), discuss the

role of fluid and impact thresholds in modeling sand and dust fluxes (Section 5), and conclude with suggestions for selecting thresholds for saltation flux predictions (Section 6).

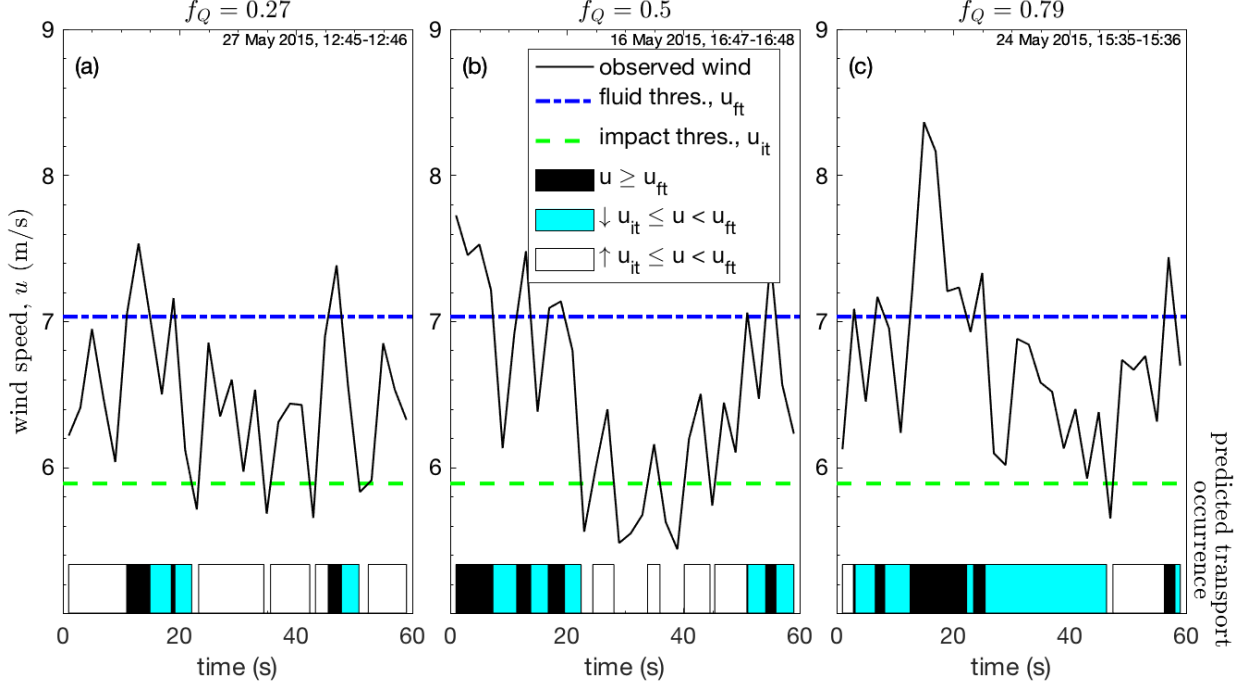


**Figure 1.** Illustration of variations in wind speed  $u$  and predicted saltation occurrence for time intervals with (a) low ( $f_Q = 0.27$ ), (b) medium ( $f_Q = 0.5$ ), and (c) high ( $f_Q = 0.79$ ) observed transport activity at Oceano. Blue and green dashed lines indicate respective fluid and impact threshold wind speeds,  $u_{ft}$  and  $u_{it}$ . Black bars at the bottom of each panel refer to times when  $u \geq u_{ft}$ . Both cyan and white bars refer to “intermittent zone” times when  $u_{it} \leq u < u_{ft}$ , but they are distinguished between times approached from above  $u_{ft}$  (cyan) versus from below  $u_{it}$  (white). Black and cyan bars thus indicate times of predicted transport occurrence. As saltation activity  $f_Q$  increases from panel a to c, the intermittent zone is increasingly approached from above and decreasingly from below.

## 2. Theory

We expect the occurrence of aeolian saltation transport to be governed by both the fluid and impact thresholds, based on the relative importance of transport initiation versus cessation. In this section, we describe how, over time intervals of intermittent saltation that include many threshold crossings, the combined contributions of  $\tau_{ft}$  and  $\tau_{it}$  should produce an intermediate “effective” threshold stress  $\tau_{th}$  that varies systematically with the fraction of time  $f_Q$  that saltation is active.

### 2.1. Regulation of saltation occurrence by fluid and impact thresholds

To illustrate the role of dual thresholds in regulating the occurrence of saltation, we consider three sample time series (Fig. 1) of near-surface horizontal wind speed  $u(t)$  straddling fluid and

impact threshold wind speeds,  $u_{ft}$  and  $u_{it}$  respectively, corresponding to  $\tau_{ft}$  and  $\tau_{it}$ . (Methods for obtaining  $u(t)$ ,  $u_{ft}$ , and  $u_{it}$  will be described in Section 3.) When  $u \geq u_{ft}$ , we unambiguously expect saltation transport to occur; conversely, when  $u < u_{it}$ , transport should not occur. Ambiguity in prediction of saltation occurrence arises in cases where  $u_{it} \leq u < u_{ft}$ . In this “intermittent zone,” saltation occurrence should depend on whether saltation transport was initiated (i.e.,  $u \geq u_{ft}$ ) more recently than it was terminated (i.e.,  $u < u_{it}$ ) [Kok, 2010b].

Over time intervals covering multiple threshold crossings, we expect the frequency of saltation activity  $f_Q$  to partially depend on the fraction of intermittent zone winds (i.e.,  $u_{it} \leq u < u_{ft}$ ) that are approached from below ( $u < u_{it}$ ) versus from above ( $u \geq u_{ft}$ ). Fig. 1 illustrates the nature of these intermittent zone events for three distinctive cases of measured infrequent (panel a:  $f_Q = 0.27$ ), moderate (panel b:  $f_Q = 0.5$ ), and frequent (panel c:  $f_Q = 0.79$ ) saltation activity.

(Methods for calculating  $f_Q$  from measurements will be described in Section 3.) When the intermittent zone is mostly approached from below (i.e., from a state of non-transport), saltation is mostly limited by the occurrence of initiation events, for which  $u \geq u_{ft}$  (Fig. 1a). As such, near the no saltation limit  $f_Q \rightarrow 0$ , saltation activity is controlled primarily by wind exceedance of the fluid threshold. In the contrasting case when the intermittent zone is mostly approached from above ( $u \geq u_{ft}$ ) (i.e., from a state of transport), saltation will mostly be sustained so long as  $u \geq u_{it}$  (Fig. 1c). Consequently, near the continuous saltation limit  $f_Q \rightarrow 1$ , saltation occurrence is controlled primarily by wind exceedance of the impact threshold. Otherwise, for cases of intermittent zone winds originating equally from starting points above  $u_{ft}$  and below  $u_{it}$  (Fig. 1b), expectations for saltation occurrence will be somewhere between these two end-member cases. In general, the examples in Fig. 1 suggest that, with an increasing fraction of intermittent zone winds originating from  $u \geq u_{ft}$  relative to  $u < u_{it}$ , saltation occurrence will move away from the  $f_Q \rightarrow 0$  limit of  $u_{ft}$  control toward the  $f_Q \rightarrow 1$  limit of  $u_{it}$  control.

## 2.2. Dual threshold hypothesis for saltation activity

The three cases presented in Fig. 1 suggest that increasing  $f_Q$  corresponds to saltation occurrence being increasingly controlled by the impact rather than the fluid threshold. Based on this observation, we consider how a statistically-defined “effective” threshold wind shear stress  $\tau_{th}$ , which refers to the average threshold wind stress above which saltation is expected to occur [e.g., *Stout and Zobeck, 1997*], reflects the relative contributions of fluid and impact threshold stresses,  $\tau_{ft}$  and  $\tau_{it}$ , with increasing  $f_Q$ . In particular, we propose a “dual threshold hypothesis”, in which  $\tau_{th} = \tau_{ft}$  in the initiation-limited rare transport case ( $f_Q \rightarrow 0$ ),  $\tau_{th} = \tau_{it}$  in the cessation-limited continuous transport case ( $f_Q \rightarrow 1$ ), and  $\tau_{th}$  decreases linearly with  $f_Q$  between these two limits:

$$\tau_{th} = f_Q \tau_{it} + (1 - f_Q) \tau_{ft}. \quad (1)$$

This hypothesis is consistent with *Schönfeldt [2004]*, who predicted an analogous gradual decrease in effective threshold with increasing mean wind speed (rather than saltation activity) in stochastic simulations of wind speed fluctuating around fluid and impact thresholds. If correct, Eq. 1 offers a way to determine the impact and fluid thresholds from measurements of effective threshold and saltation activity. Conversely, Eq. 1 could also allow for prediction of saltation activity from wind time series and known impact and fluid thresholds.

### 3. Methods

To evaluate our dual threshold hypothesis that effective threshold is partitioned between fluid and impact thresholds depending on the saltation activity (Eq. 1), we analyzed simultaneous high-frequency measurements of active saltation and wind at three field sites (Jericoacoara, Rancho Guadalupe, and Oceano) with distinctive soil conditions. Multiple (3-9) Wenglor optical sensors [Barchyn *et al.*, 2014a] at heights from the bed surface up to  $\approx 0.3$  m counted saltating particles (at 25 Hz), which we converted to vertically-integrated saltation particle count rates  $N$  (Fig. 2a). A sonic anemometer at height  $z_U \approx 0.5$  m measured wind velocity (25 Hz at Jericoacoara and Rancho Guadalupe, 50 Hz at Oceano) (Fig. 2d). Though our field deployments (described further in Martin *et al.* [2017]) included anemometers at multiple heights, we chose to use measurements from only the lowest anemometer (i.e.,  $z_U \approx 0.5$  m) at each site, because we expected these measurements to be most representative of wind fluctuations at the sand surface.

To calculate saltation activity  $f_Q$  and effective threshold wind speed  $u_{th}$ , we applied  $\delta t = 2$  s interval averaging to saltation (Fig. 2b) and wind (Fig. 2e) time series, then we subdivided these data into  $\Delta t = 1$  minute analysis intervals. Within each analysis interval, we calculated saltation activity  $f_Q$  as the fraction of  $\delta t$  increments within  $\Delta t$  for which  $N$  was nonzero (Fig 2c) and applied a correction (see Supporting Information Text S1) to account for the possibility of false negatives. For each  $\Delta t$ , we then calculated effective threshold wind speed  $u_{th}$  by applying the “Time Frequency Equivalence Method” [Stout and Zobeck, 1997; Stout, 2004; Wiggs *et al.*, 2004b]:

$$u_{th} = \Phi_u(1 - f_Q), \quad (2)$$

where  $\Phi_u(1 - f_Q)$  is the value in the cumulative distribution of wind speeds  $\Phi_u$  corresponding to the time fraction of inactive saltation,  $1 - f_Q$  (Fig. 2f). When calculating  $\Phi_u$  for each  $\Delta t$ , we used the  $\delta t$ -averaged  $u$  values, in correspondence with our methods for calculating  $f_Q$ . We chose the averaging interval  $\delta t = 2$  s based on the typical response time of saltation to turbulent wind fluctuations [e.g., Anderson and Haff, 1988; McEwan and Willetts, 1991; Ma and Zheng, 2011], and we chose the analysis interval  $\Delta t = 1$  minute to represent the typical oscillation period for large-scale structures in an atmospheric boundary layer [e.g., Guala *et al.*, 2011]. We note here that, due to the spatial separation of wind and saltation measurements, we did not attempt to directly relate individual wind gusts to individual occurrences of saltation. Instead, we assumed that measured wind fluctuations over  $\Delta t$  are statistically representative of the wind experienced by the measured saltating particles.

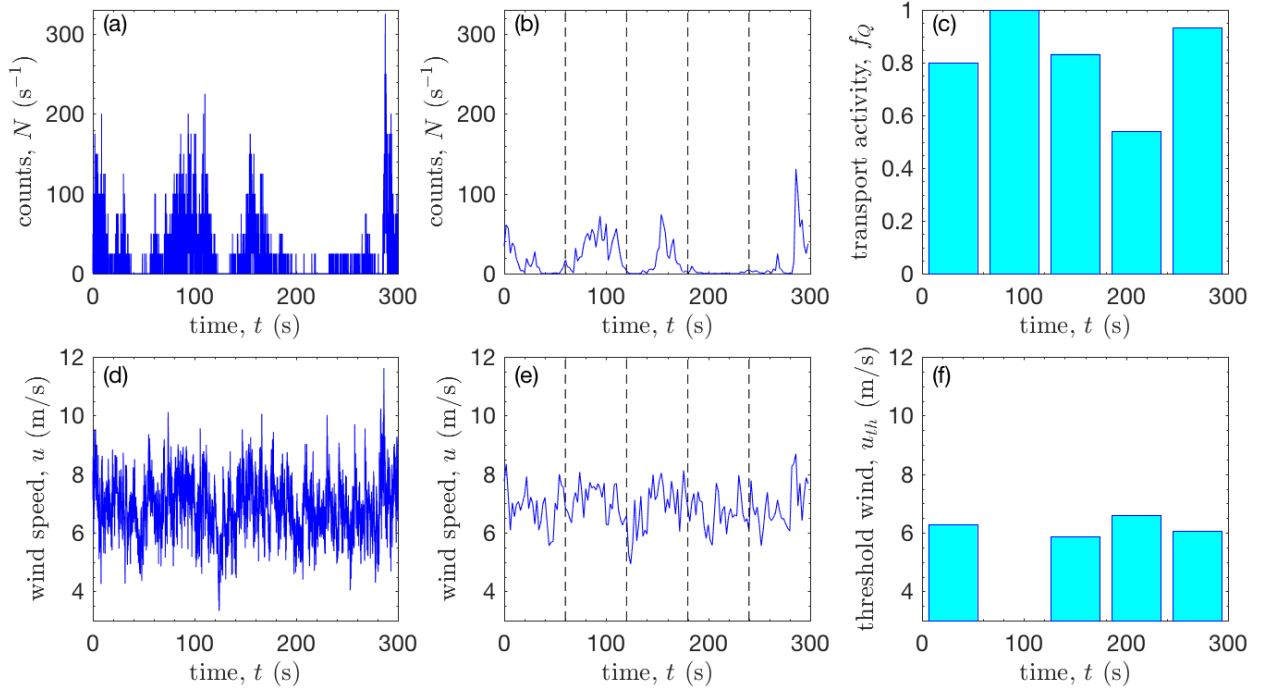


**Figure 2.** Sample measurements (Rancho Guadalupe, 24 March 2015, 13:31-13:36) to illustrate methods for calculating saltation transport activity  $f_Q$  and effective threshold wind speed  $u_{th}$ . (a) Time series of total particle counts rate  $N$ . (b)  $\delta t = 2$ s interval-averaged  $N$  time series. Dashed lines indicate  $\Delta t = 1$  minute analysis intervals. (c) Transport activities  $f_Q$ , calculated as fraction of  $\delta t$  increments in each  $\Delta t$  for which  $N > 0$ , and corrected for false negatives. (d) Time series of streamwise wind speed  $u$ . (e)  $\delta t = 2$ s interval-averaged  $u$ . Dashed lines again indicate  $\Delta t$ . (f) Resulting values of threshold wind speed  $u_{th}$  calculated by Eq. 2 from corresponding  $f_Q$  and wind speed distributions  $\Phi_u$  for each  $\Delta t$ .  $u_{th}$  is undefined for  $t = 60$ -120s when  $f_Q = 1$ .

We converted effective threshold wind speeds  $u_{th}$  to effective threshold shear velocities  $u_{*,th}$  and stresses  $\tau_{th}$  by the law-of-the-wall and the standard  $\tau$ - $u_*$  relationship:

$$u_{th} = \frac{u_{*,th}}{\kappa} \ln \left( \frac{z_u}{z_0} \right), \quad (3)$$

$$\tau_{th} = \rho_f u_{*,th}^2, \quad (4)$$

where  $z_0$  is aerodynamic roughness height,  $\kappa \approx 0.4$  is the von Karman parameter,  $\rho_f$  is air density, and  $u_{th}$  values were grouped into  $f_Q$  bins to facilitate uncertainty estimation (see Supporting Information Text S2). To justify use of the law-of-the-wall, which only applies to unidirectional and neutrally-stable conditions, our threshold calculations included only intervals with stability parameter  $|z/L| \leq 0.2$ , below which law-of-the-wall and Reynolds stress estimates of shear stress are roughly equivalent [Salesky *et al.*, 2012], and with wind direction  $|\theta| \leq 20^\circ$ , where  $\theta = 0^\circ$  is the mean sediment-transporting wind (see Martin and Kok [2017] for further explanation). Though effective  $z_0$  [e.g., Sherman, 1992] and possibly  $\kappa$  [Li *et al.*, 2010] are known to change with saltation intensity, we assumed constant  $z_0$  and  $\kappa$  in all calculations, based on a negligible observed change in  $z_0$  with  $f_Q$  (see Supporting Information Text S3).

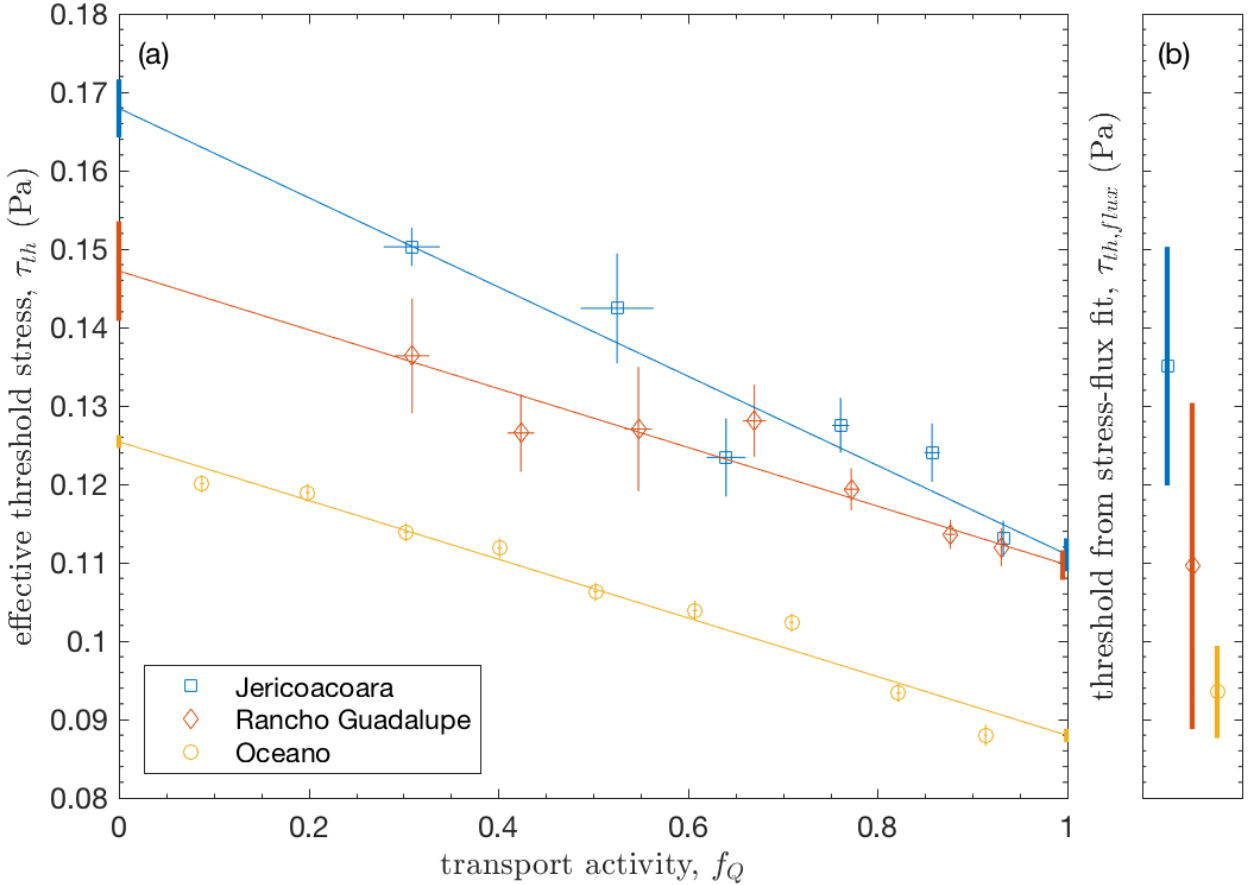


**Figure 3.** (a) Effective threshold stress  $\tau_{th}$  versus saltation transport activity  $f_Q$ . Color-coded lines show least-squares fits to Eq. 1 at each field site. Vertical bars at  $f_Q = 0$  and  $f_Q = 1$  denote respective estimates of the fluid threshold  $\tau_{ft}$  and impact threshold  $\tau_{it}$  from the linear fit. (b) Thresholds  $\tau_{th,flux}$  were estimated by applying Eq. 5 to saltation flux measurements reported in *Martin and Kok [2017]*. Specific values for  $\tau_{ft}$ ,  $\tau_{it}$ , and  $\tau_{th,flux}$  are listed in Supporting Information Table S1. Error bars correspond to 1 standard error.

## 4. Results

To evaluate our hypothesis for dual threshold control of saltation activity and the effective saltation threshold (Eq. 1), we use the methods described in Section 3 to calculate effective threshold stresses and saltation activities at our three field sites. Due to the distinctive soil properties at each field site, we analyze the effective thresholds and saltation activities for each site separately.

As predicted by Eq. 1, we find that the effective threshold stress  $\tau_{th}$  decreases linearly with saltation activity  $f_Q$  at each of the field sites (Fig. 3a). Fitting regression lines to the measurements in Fig. 3a, we find that the observed decline in  $\tau_{th}$  with  $f_Q$  is extremely unlikely by random chance alone ( $p < 10^{-6}$ ). Based on Eq. 1, we calculate fluid and impact threshold stresses,  $\tau_{ft}$  and  $\tau_{it}$ , from the limiting effective threshold values for no transport ( $f_Q \rightarrow 0$ ) and continuous transport ( $f_Q \rightarrow 1$ ) for the linear regressions. These calculated  $\tau_{ft}$  and  $\tau_{it}$  are

comparable to values from wind tunnel experiments for similar grain sizes [see Figs. 5 and 21 in *Kok et al.*, 2012]. Converting fluid and impact threshold stresses to threshold shear velocities by Eq. 4, we calculate threshold ratios  $u_{*,it}/u_{*,ft} = 0.813 \pm 0.018$ ,  $0.863 \pm 0.027$ , and  $0.837 \pm 0.007$  at Jericoacoara, Rancho Guadalupe, and Oceano, respectively, which are consistent with laboratory measurements [*Bagnold*, 1937] and numerical predictions [*Kok*, 2010a] of  $u_{*,it}/u_{*,ft} \approx 0.82$  (i.e.,  $\tau_{it}/\tau_{ft} \approx 0.67$ ) (See Supporting Information Text S4).

These results support our hypothesis that the dual thresholds and saltation activity interact to determine the effective threshold (Eq. 1). In particular, we found that observed values of fluid and impact thresholds (Fig. 3) agree with numerical and experimental expectations. This agreement supports our interpretation that fluid threshold indeed dominates in the rare transport limit ( $f_Q \rightarrow 0$ ), while impact threshold dominates in the continuous transport limit ( $f_Q \rightarrow 1$ ). Eq. 1 thus provides a framework for estimating fluid and impact thresholds for a specific field site based on measurements of intermittent saltation. As we discuss below, our findings also inform the prediction of saltation transport using wind measurements over soils with known or estimated threshold values.

## 5. Discussion

Our results provide the first field-based evidence for the existence of separate fluid and impact thresholds in aeolian saltation. Though fluid and impact thresholds for saltation initiation and cessation have long been theorized [e.g., *Bagnold*, 1937; *Kok*, 2010b] and measured in wind tunnel experiments [e.g., *Iversen and Rasmussen*, 1994], the difficulty of directly measuring threshold crossings in the field [e.g., *Barchyn and Hugenholtz*, 2011] has limited the ability of past studies to resolve both thresholds. To overcome these limitations, we hypothesized, based on observations (Fig. 1), that the relative contributions of fluid and impact thresholds to saltation occurrence vary systematically with the frequency of saltation transport (Eq. 1). As expected from this dual threshold hypothesis, we observed that the statistically-defined effective threshold stress [*Stout and Zobeck*, 1997; *Stout*, 2004] (Fig. 2) decreases linearly with saltation activity (Fig. 3). Based on the limiting effective threshold values for rare and near-continuous saltation, we then calculated distinct fluid and impact threshold stresses at the three field sites, which we found to be consistent with past theory and experiments.

Our observations offer two primary pieces of evidence supporting the combined role of distinctive fluid and impact thresholds in controlling saltation occurrence. First, a systematic decrease in effective threshold with increasing saltation activity is consistent with our dual threshold hypothesis (Eq. 1), which predicts a gradual shift from fluid threshold to impact threshold control with increasing transport activity. Second, our estimated values for impact and fluid threshold are consistent with predicted ratios of these values and independent estimates of impact threshold versus grain size. These pieces of evidence thus also lend support to our statistically-based approach for determining fluid and impact thresholds from field measurements of wind speed and saltation activity.

Despite this evidence supporting the existence of dual thresholds, we consider aspects of our method that could have produced an artificial variation in effective threshold with saltation activity. First, our findings could depend on the selection of averaging intervals  $\delta t$  (Fig. 2) [*Stout*, 1998; *Wiggs et al.*, 2004b; *Barchyn and Hugenholtz*, 2011]. Saltation is more likely to

occur within longer  $\delta t$  increments (Fig. 2b), thus increasing  $f_Q$  (Fig. 2c). Longer  $\delta t$  also decreases the amplitude of wind fluctuations (Fig. 2e), which reduces the range of measured effective thresholds  $u_{th}$  (Fig. 2f). To evaluate these effects for a range of  $\delta t$  (1-4 seconds) corresponding to typical saltation response times [e.g., *Anderson and Haff*, 1988; *McEwan and Willetts*, 1991; *Ma and Zheng*, 2011], we performed a sensitivity analysis (Supporting Information Text S5). Though  $\tau_{it}$ ,  $\tau_{ft}$ , and  $u_{*it}/u_{*ft}$  do vary with  $\delta t$ , these calculations remain broadly consistent with independent measurements [*Bagnold*, 1937; *Kok*, 2010b] regardless of  $\delta t$ . Second, our findings could also depend on the selection of analysis interval  $\Delta t$ , but sensitivity analyses found no systematic trends with  $\Delta t$  (Supporting Information Text S5). Third, it is possible that increasing momentum extraction by the saltation cloud with increasing saltation intensity [i.e., *Sherman*, 1992] could have biased our calculations, which assume constant roughness height  $z_0$  (Eq. 3). However, we found no systematic variation in  $z_0$  with transport activity  $f_Q$  (Supporting Information Text S3), indicating that such bias is unlikely to have affected our results.

Other factors, such as grain size [*Wiggs et al.*, 2004b; *Stout*, 2007], soil moisture [*Stout*, 2004; *Wiggs et al.*, 2004a; *Davidson-Arnott et al.*, 2005, 2008], and turbulence properties [*McKenna Neuman et al.*, 2000; *Davidson-Arnott et al.*, 2005], could have also played a role in the observed variations in effective threshold. To investigate these factors, we performed sensitivity analyses by date (a proxy for grain size, which coarsened through time at Oceano), and time of day (a proxy for soil moisture and atmospheric stability), but found no systematic trends for these factors (Supporting Information Text S6). Differences in grain size distributions do produce differences in effective thresholds among sites (Fig. 3a), but these differences are consistent with expected impact and fluid thresholds [e.g., *Kok et al.*, 2012] for the soil particle size distributions at each site. Nonetheless, further work is needed to understand the sensitivity of thresholds to atmospheric stability [e.g., *Frank and Kocurek*, 1994], soil texture [e.g., *Greeley and Iversen*, 1985], soil moisture [e.g., *Davidson-Arnott et al.*, 2008] and other soil conditions [e.g., *Webb et al.*, 2016].

Recent wind tunnel measurements support our interpretations of how fluid and impact thresholds govern saltation transport. *Walter et al.* [2014] found that, so long as saltation activity is continuous (i.e.,  $f_Q = 1$ ), bed surface shear stress  $\tau_0$  remains constant with changes in  $Q$ . By *Owen's hypothesis* [*Owen*, 1964], *Walter et al.* interpreted this constant  $\tau_0$  as implying a constant rate of wind momentum dissipation at the bed surface equal to the impact threshold stress  $\tau_{it}$ . However, they also observed  $\tau_0$  to decrease monotonically from  $\tau_{ft}$  to  $\tau_{it}$  during the transition from no saltation to continuous saltation [Fig. 4 in *Walter et al.*, 2014], suggesting that  $\tau_0$ , like effective threshold  $\tau_{th}$ , is governed by changes in  $f_Q$  modulating the relative importance of fluid and impact thresholds. *Paterna et al.* [2016] further observed that transport initiation events during weak saltation are dominantly related to energetic turbulent eddies (i.e., fluid entrainment). In contrast, as saltation strengthens, variations in saltation flux decouple from the occurrence of turbulence structures, as the splash process (i.e., impact entrainment) plays an increasing role in sustaining saltation and transporting momentum to the bed surface. These findings that the processes governing wind momentum transfer [*Paterna et al.*, 2016] and dissipation [*Walter et al.*, 2014] during saltation display fluid threshold control during weak saltation and impact threshold control during intense saltation are consistent with our dual

threshold hypothesis (Eq. 1) relating fluid to impact threshold contributions to the saltation activity.

Based on Eq. 1 and this recent wind tunnel work, we expect impact threshold to dominate saltation dynamics in the limit of continuous ( $f_Q = 1$ ) transport associated with moderate to strong saltation. We can gain insight into the importance of this continuous transport impact threshold control in saltation flux modeling by comparing fluid and impact threshold stresses calculated here to independent “flux-based” threshold stresses  $\tau_{th,flux}$ . These were obtained by *Martin and Kok* [2017] from the zero-intercept of the linear fit to saltation flux  $Q$  versus shear stress  $\tau$ , i.e.,

$$Q \propto (\tau - \tau_{th,flux}). \quad (5)$$

Notably, values for  $\tau_{th,flux}$  agree with our  $\tau_{it}$  measurements within  $2\sigma$  uncertainty ranges, and in all cases  $\tau_{th,flux}$  values are closer to  $\tau_{it}$  than to  $\tau_{ft}$  (Fig. 3). We explain this general agreement between  $\tau_{th,flux}$  and  $\tau_{it}$  by the fact that most observed saltation at our field sites occurred under continuous or near-continuous transport conditions, for which  $\tau_{it}$  dominantly controls wind momentum dissipation [Walter *et al.*, 2014] and the zero-intercept of the flux law [Martin and Kok, 2017]. Due to the relatively narrow range of shear stresses for which saltation is intermittent (roughly  $\tau/\tau_{it} = 1 - 1.5$ , Supporting Information Fig. S1), which is small compared to the range of  $\tau/\tau_{it} = \sim 1 - 4$  over which saltation is observed at our field sites and those reported in the literature [Greeley *et al.*, 1996; Namikas, 2003; Li *et al.*, 2010; Farrell *et al.*, 2012], we expect most saltation on Earth to be continuous and thus governed by  $\tau_{it}$ . Therefore, while  $\tau_{ft}$  may merely serve as a rough boundary between intermittent and continuous saltation (Supporting Information Fig. S1),  $\tau_{it}$  alone can serve as the *de facto* saltation threshold in studies modeling saltation flux over longer time intervals (i.e., 30 minutes). In such studies,  $\tau_{it}$  could be estimated by its known relationship with median grain diameter for dry soils [e.g., Kok *et al.*, 2012]. However, when the gap between fluid and impact thresholds is large, as on Mars and several other planetary bodies [Pähzt and Durán, 2017], and intermittent (rather than continuous) transport is the dominant mode of saltation [Kok, 2010b],  $\tau_{ft}$  and  $\tau_{it}$  may need to be included together in saltation flux models. In such cases where direct measurements of  $\tau_{ft}$  and  $\tau_{it}$  are not possible, these thresholds could be estimated from theoretical relationships [e.g., Claudin and Andreotti, 2006; Kok, 2010b], numerical models [e.g., Kok, 2010a], or experimental studies [e.g., Iversen and White, 1982].

Our findings offer insight into how the threshold should be incorporated into models for sand and dust flux. Both fluid and impact threshold should be used together when considering high-frequency saltation fluctuations, for which the flux-based threshold appears to be partially governed by averaging timescale [Martin *et al.*, 2013]. Dual thresholds should also be considered for modeling saltation on Mars [Kok, 2010b] or other planetary bodies [Pähzt and Durán, 2017] where the gap between fluid and impact thresholds is much larger than on Earth. However, when modeling saltation flux over longer analysis intervals (i.e., 30 minutes), such as in large-scale models for wind erosion [e.g., Chepil, 1945], dune migration [e.g., Fryberger *et al.*, 1979], and dust emission [e.g., Gillette and Passi, 1988], our results indicate that use of the impact threshold alone is sufficient. For the  $\tau/\tau_{it} \approx 1 - 4$  range over which we observe saltation (Supporting Information Fig. S1), the choice of impact versus fluid threshold for saltation modeling (i.e., by Eq. 5) will produce at least a 10% difference in the prediction for saltation flux (and a  $>50\%$

difference for  $\tau/\tau_{it} < 2$ ). Therefore, adoption of the impact threshold, instead of the commonly-used higher fluid threshold [e.g., *Iversen and White*, 1982; *Marticorena and Bergametti*, 1995; *Shao*, 2008], could improve predictions for saltation flux. Since the dust emission flux is generally modeled as proportional to the saltation flux [e.g., *Marticorena and Bergametti*, 1995; *Shao*, 2008; *Kok et al.*, 2012], our findings have the potential to also improve predictions of dust emission fluxes.

## 6. Conclusion

Here we offered the first field-based evidence of distinct fluid and impact thresholds for the respective initiation and cessation of aeolian saltation. The measured ratio of these thresholds is consistent with past laboratory and numerical studies of dual thresholds. We calculated fluid and impact thresholds by examining their roles in regulating saltation activity. When saltation is active a small fraction of the time, wind exceedance of fluid threshold controls saltation occurrence. As saltation activity increases, so too does the influence of the impact threshold, until saltation occurrence is controlled mostly by wind exceedance of impact threshold under near-continuous transport conditions. Although dual thresholds are thus required for certain saltation modeling applications, our results indicate that the impact threshold alone is sufficient for predicting the time-averaged ( $\sim 30$  mins) saltation flux on Earth. Consequently, we suggest that parameterizations of sand and dust transport in aeolian process models, which currently predominantly use the fluid threshold, should instead adopt the impact threshold for predictions.

**ACKNOWLEDGEMENTS.** U.S. National Science Foundation (NSF) Postdoctoral Fellowship EAR-1249918 to R.L.M. and NSF grant AGS-1358621 to J.F.K. supported this research. Research was also sponsored by the Army Research Laboratory and was accomplished under Grant Number W911NF-15-1-0417. The views and conclusions contained in this document are those of the authors and should not be interpreted as representing the official policies, either expressed or implied, of the Army Research Laboratory or the U.S. Government. The U.S. Government is authorized to reproduce and distribute reprints for Government purposes notwithstanding any copyright notation herein. Oceano Dunes State Vehicular Recreation Area, Rancho Guadalupe Dunes Preserve, and Jericoacoara National Park provided essential site access and support. Jericoacoara fieldwork is registered with the Brazilian Ministry of the Environment (#46254-1 to J. Ellis). We thank Marcelo Chamecki for advice on treatment of wind data, Chris Hugenholtz and Tom Barchyn for equipment help, Doug Jerolmack for lab access for grain-size analysis, and Jean Ellis, Paulo Sousa, Peter Li, Francis Turney, Arkayan Samaddar, and Livia Freire for field assistance. We also thank the two anonymous reviewers for their thoughtful suggestions on the original and revised manuscripts. Data included in the analysis for this paper is described in Supporting Information Dataset S1 and can be found on the Zenodo data repository at <http://doi.org/10.5281/zenodo.574896>.

## References

Anderson, R. S., and P. K. Haff (1988), Simulation of eolian saltation, *Science*, 241(4867), 820–823, doi:10.1126/science.241.4867.820.

Ayoub, F., J.-P. Avouac, C. E. Newman, M. I. Richardson, A. Lucas, S. Leprince, and N. T. Bridges (2014), Threshold for sand mobility on Mars calibrated from seasonal variations of sand flux, *Nat. Commun.*, 5, 5096.

Baas, A. C. W. (2008), Challenges in aeolian geomorphology: Investigating aeolian streamers, *Geomorphology*, 93(1–2), 3–16, doi:10.1016/j.geomorph.2006.12.015.

Bagnold, R. A. (1937), The transport of sand by wind, *Geogr. J.*, 89(5), 409–438, doi:10.2307/1786411.

Bagnold, R. A. (1941), *The Physics of Blown Sand and Desert Dunes*, Dover, London.

Barchyn, T. E., and C. H. Hugenholtz (2011), Comparison of four methods to calculate aeolian sediment transport threshold from field data: Implications for transport prediction and discussion of method evolution, *Geomorphology*, 129(3–4), 190–203, doi:10.1016/j.geomorph.2011.01.022.

Barchyn, T. E., C. H. Hugenholtz, B. Li, C. McKenna Neuman, and R. S. Sanderson (2014a), From particle counts to flux: Wind tunnel testing and calibration of the “Wenglor” aeolian sediment transport sensor, *Aeolian Res.*, 15, 311–318, doi:10.1016/j.aeolia.2014.06.009.

Barchyn, T. E., R. L. Martin, J. F. Kok, and C. H. Hugenholtz (2014b), Fundamental mismatches between measurements and models in aeolian sediment transport prediction: The role of small-scale variability, *Aeolian Res.*, 15, 245–251, doi:10.1016/j.aeolia.2014.07.002.

Bevington, P. R., and D. K. Robinson (2003), *Data reduction and error analysis for the physical sciences*, 3rd ed., McGraw-Hill, New York.

van Boxel, J. H., G. Sterk, and S. M. Arens (2004), Sonic anemometers in aeolian sediment transport research, *Geomorphology*, 59(1–4), 131–147, doi:10.1016/j.geomorph.2003.09.011.

Bridges, N. T., F. Ayoub, J.-P. Avouac, S. Leprince, A. Lucas, and S. Mattson (2012), Earth-like sand fluxes on Mars, *Nature*, 485(7398), 339–342, doi:10.1038/nature11022.

Carneiro, M. V., K. R. Rasmussen, and H. J. Herrmann (2015), Bursts in discontinuous Aeolian saltation, *Sci. Rep.*, 5, doi:10.1038/srep11109.

Chepil, W. S. (1945), Dynamics of Wind Erosion. 2. Initiation of soil movement, *Soil Sci.*, 60(5), 397, doi:10.1097/00010694-194511000-00005.

Claudin, P., and B. Andreotti (2006), A scaling law for aeolian dunes on Mars, Venus, Earth, and for subaqueous ripples, *Earth Planet. Sci. Lett.*, 252(1–2), 30–44, doi:10.1016/j.epsl.2006.09.004.

Creyssels, M., P. Dupont, A. O. El Moctar, A. Valance, I. Cantat, J. T. Jenkins, J. M. Pasini, and K. R. Rasmussen (2009), Saltating particles in a turbulent boundary layer: Experiment and theory, *J. Fluid Mech.*, 625, 47–74, doi:10.1017/S0022112008005491.

Davidson-Arnott, R. G. D., K. MacQuarrie, and T. Aagaard (2005), The effect of wind gusts, moisture content and fetch length on sand transport on a beach, *Geomorphology*, 68(1–2), 115–129, doi:10.1016/j.geomorph.2004.04.008.

Davidson-Arnott, R. G. D., Y. Yang, J. Ollerhead, P. A. Hesp, and I. J. Walker (2008), The effects of surface moisture on aeolian sediment transport threshold and mass flux on a beach, *Earth Surf. Process. Landf.*, 33(1), 55–74, doi:10.1002/esp.1527.

Farrell, E. J., D. J. Sherman, J. T. Ellis, and B. Li (2012), Vertical distribution of grain size for wind blown sand, *Aeolian Res.*, 7, 51–61, doi:10.1016/j.aeolia.2012.03.003.

Frank, A., and G. Kocurek (1994), Effects of atmospheric conditions on wind profiles and aeolian sand transport with an example from White Sands National Monument, *Earth Surf. Process. Landf.*, 19(8), 735–745, doi:10.1002/esp.3290190806.

Fryberger, S. G., G. Dean, and E. D. McKee (1979), Dune forms and wind regime, in *A Study of Global Sand Seas, U.S. Geological Survey Professional Paper 1052, E. D. McKee, Ed.*, pp. 137–170.

Gillette, D. A., and R. Passi (1988), Modeling dust emission caused by wind erosion, *J. Geophys. Res. Atmospheres*, 93(D11), 14233–14242, doi:10.1029/JD093iD11p14233.

Greeley, R., and J. D. Iversen (1985), *Wind as a Geological Process on Earth, Mars, Venus and Titan*, Cambridge University Press, New York.

Greeley, R., D. G. Blumberg, and S. H. Williams (1996), Field measurements of the flux and speed of wind-blown sand, *Sedimentology*, 43(1), 41–52, doi:10.1111/j.1365-3091.1996.tb01458.x.

Guala, M., M. Metzger, and B. J. McKeon (2011), Interactions within the turbulent boundary layer at high Reynolds number, *J. Fluid Mech.*, 666, 573–604, doi:10.1017/S0022112010004544.

Ho, T. D., A. Valance, P. Dupont, and A. Ould El Moctar (2011), Scaling laws in aeolian sand transport, *Phys. Rev. Lett.*, 106(9), 94501, doi:10.1103/PhysRevLett.106.094501.

Iversen, J. D., and K. R. Rasmussen (1994), The effect of surface slope on saltation threshold, *Sedimentology*, 41(4), 721–728, doi:10.1111/j.1365-3091.1994.tb01419.x.

Iversen, J. D., and B. R. White (1982), Saltation threshold on Earth, Mars and Venus, *Sedimentology*, 29(1), 111–119, doi:10.1111/j.1365-3091.1982.tb01713.x.

Kok, J. F. (2010a), An improved parameterization of wind-blown sand flux on Mars that includes the effect of hysteresis, *Geophys. Res. Lett.*, 37(12), L12202, doi:10.1029/2010GL043646.

Kok, J. F. (2010b), Difference in the wind speeds required for initiation versus continuation of sand transport on Mars: Implications for dunes and dust storms, *Phys. Rev. Lett.*, 104(7), 74502, doi:10.1103/PhysRevLett.104.074502.

Kok, J. F., E. J. R. Parteli, T. I. Michaels, and D. B. Karam (2012), The physics of wind-blown sand and dust, *Rep. Prog. Phys.*, 75, 106901, doi:10.1088/0034-4885/75/10/106901.

Kok, J. F. et al. (2014), An improved dust emission model – Part 1: Model description and comparison against measurements, *Atmos Chem Phys*, 14(23), 13023–13041, doi:10.5194/acp-14-13023-2014.

Li, B., D. J. Sherman, E. J. Farrell, and J. T. Ellis (2010), Variability of the apparent von Karman parameter during aeolian saltation, *Geophys. Res. Lett.*, 37(15), L15404, doi:10.1029/2010GL044068.

Li, Z., X. Zhao, and W. Huang (2008), A stochastic model for initial movement of sand grains by wind, *Earth Surf. Process. Landf.*, 33(11), 1796–1803, doi:10.1002/esp.1638.

Lindhorst, S., and C. Betzler (2016), The climate-archive dune: Sedimentary record of annual wind intensity, *Geology*, 44(9), 711–714, doi:10.1130/G38093.1.

Lorenz, R. D., and J. R. Zimbelman (2014), *Dune Worlds*, Springer, Heidelberg.

Ma, G. S., and X. J. Zheng (2011), The fluctuation property of blown sand particles and the wind-sand flow evolution studied by numerical method, *Eur. Phys. J. E*, 34(5), doi:10.1140/epje/i2011-11054-3.

Marticorena, B., and G. Bergametti (1995), Modeling the atmospheric dust cycle: 1. Design of a soil-derived dust emission scheme, *J. Geophys. Res. Atmospheres*, 100(D8), 16415–16430, doi:10.1029/95JD00690.

Martin, R. L., and J. F. Kok (2017), Wind-invariant saltation heights imply linear scaling of aeolian saltation flux with shear stress, *Sci. Adv.* (Accepted Manuscript).

Martin, R. L., T. E. Barchyn, C. H. Hugenholtz, and D. J. Jerolmack (2013), Timescale dependence of aeolian sand flux observations under atmospheric turbulence, *J. Geophys. Res. Atmospheres*, 118(16), 9078–9092, doi:10.1002/jgrd.50687.

Martin, R. L., J. F. Kok, and M. Chamecki (2017), Comprehensive field campaigns illustrate new methods for characterizing high-frequency variability in aeolian saltation flux, *arXiv:1609.08707v2*.

McEwan, I. K., and B. B. Willetts (1991), Numerical model of the saltation cloud., *Acta Mech. Suppl.*, 1, 53–66.

McKenna Neuman, C., N. Lancaster, and W. G. Nickling (2000), The effect of unsteady winds on sediment transport on the stoss slope of a transverse dune, Silver Peak, NV, USA, *Sedimentology*, 47(1), 211, doi:10.1046/j.1365-3091.2000.00289.x.

Namikas, S. L. (2003), Field measurement and numerical modelling of aeolian mass flux distributions on a sandy beach, *Sedimentology*, 50(2), 303–326, doi:10.1046/j.1365-3091.2003.00556.x.

Nickling, W. G. (1988), The initiation of particle movement by wind, *Sedimentology*, 35(3), 499–511, doi:10.1111/j.1365-3091.1988.tb01000.x.

Owen, P. R. (1964), Saltation of uniform grains in air, *J. Fluid Mech.*, 20(2), 225–242, doi:10.1017/S0022112064001173.

Pähzt, T., and O. Durán (2017), Fluid forces or impacts, what governs the entrainment of soil particles in sediment transport mediated by a Newtonian fluid?, *arXiv:1605.07306v5*.

Paterna, E., P. Crivelli, and M. Lehning (2016), Decoupling of mass flux and turbulent wind fluctuations in drifting snow, *Geophys. Res. Lett.*, 43(9), 2016GL068171, doi:10.1002/2016GL068171.

Rice, M. A., I. K. McEwan, and C. E. Mullins (1999), A conceptual model of wind erosion of soil surfaces by saltating particles, *Earth Surf. Process. Landf.*, 24(5), 383–392, doi:10.1002/(SICI)1096-9837(199905)24:5<383::AID-ESP995>3.0.CO;2-K.

Salesky, S. T., M. Chamecki, and N. L. Dias (2012), Estimating the random error in eddy-covariance based fluxes and other turbulence statistics: the filtering method, *Bound.-Layer Meteorol.*, 144(1), 113–135, doi:10.1007/s10546-012-9710-0.

Schönfeldt, H. J. (2004), Establishing the threshold for intermittent aeolian sediment transport., *Meteorol. Z.*, 13(5), 437–444, doi:10.1127/0941-2948/2004/0013-0437.

Shao, Y. (2008), *Physics and Modelling of Wind Erosion*, Springer, The Netherlands.

Shao, Y., and H. Lu (2000), A simple expression for wind erosion threshold friction velocity, *J. Geophys. Res.*, 105(D17), 22437–22443, doi:200010.1029/2000JD900304.

Sherman, D. J. (1992), An equilibrium relationship for shear velocity and apparent roughness length in aeolian saltation, *Geomorphology*, 5(3–5), 419–431, doi:10.1016/0169-555X(92)90016-H.

Sherman, D. J., B. Li, J. T. Ellis, E. J. Farrell, L. P. Maia, and H. Granja (2013), Recalibrating aeolian sand transport models, *Earth Surf. Process. Landf.*, 38(2), 169–178, doi:10.1002/esp.3310.

Stout, J. E. (1998), Effect of averaging time on the apparent threshold for aeolian transport, *J. Arid Environ.*, 39(3), 395–401, doi:10.1006/jare.1997.0370.

Stout, J. E. (2004), A method for establishing the critical threshold for aeolian transport in the field, *Earth Surf. Process. Landf.*, 29(10), 1195–1207, doi:10.1002/esp.1079.

Stout, J. E. (2007), Simultaneous observations of the critical aeolian threshold of two surfaces, *Geomorphology*, 85(1–2), 3–16, doi:10.1016/j.geomorph.2006.03.034.

Stout, J. E., and T. M. Zobeck (1997), Intermittent saltation, *Sedimentology*, 44(5), 959–970, doi:10.1046/j.1365-3091.1997.d01-55.x.

Ungar, J. E., and P. K. Haff (1987), Steady state saltation in air, *Sedimentology*, 34(2), 289–299, doi:10.1111/j.1365-3091.1987.tb00778.x.

Walter, B., S. Horender, C. Voegeli, and M. Lehning (2014), Experimental assessment of Owen's second hypothesis on surface shear stress induced by a fluid during sediment saltation, *Geophys. Res. Lett.*, 41(17), 6298–6305, doi:10.1002/2014GL061069.

Webb, N. P., M. S. Galloza, T. M. Zobeck, and J. E. Herrick (2016), Threshold wind velocity dynamics as a driver of aeolian sediment mass flux, *Aeolian Res.*, 20, 45–58.

Wiggs, G. F. S., A. J. Baird, and R. J. Atherton (2004a), The dynamic effects of moisture on the entrainment and transport of sand by wind, *Geomorphology*, 59(1–4), 13–30, doi:10.1016/j.geomorph.2003.09.002.

Wiggs, G. F. S., R. J. Atherton, and A. J. Baird (2004b), Thresholds of aeolian sand transport: establishing suitable values, *Sedimentology*, 51(1), 95–108, doi:10.1046/j.1365-3091.2003.00613.x.

Supporting Information for

**Field measurements demonstrate distinct initiation and cessation thresholds  
governing aeolian sediment transport flux**

Raleigh L. Martin<sup>1</sup> and Jasper F. Kok<sup>1</sup>

<sup>1</sup>Department of Atmospheric and Oceanic Sciences, University of California, Los Angeles, CA 90095

**Contents of this file**

Text S1 to S7

Figures S1 to S8

Tables S1 to S5

**Additional Supporting Information (Files available separately)**

Caption for Dataset S1

**Introduction**

In this supporting document, we describe details associated with the analyses presented in the main paper. Text S1 describes a correction to account for false negatives when calculating saltation activity, Text S2 explains methods for calculating and propagating uncertainty in threshold estimates, Text S3 presents calculations for the roughness height used to convert wind speed to shear stress, Text S4 details methods for computing fluid and impact thresholds, Text S5 justifies our choices of averaging and analysis intervals, Text S6 considers the possibility of diurnal or secular trends affecting threshold variability, and Text S7 lists variables used in the main paper and Supporting Information Text. Supporting Figures (S1-S8) and Tables (S1-S5) accompany this text. In addition, we describe Supporting Dataset S1, which contains the threshold and saltation activity values calculated for this analysis.

## Text S1. Accounting for false negatives in calculation of saltation activity

Here, we derive a method to account for the possibility of “false negatives” (i.e., instances in which saltation transport occurs but is not detected) when computing saltation activity  $f_Q$ . To do so, we distinguish the measured saltation detection rate  $f_D$  from the actual saltation activity  $f_Q$ . We compute  $f_D$  as the fraction of averaging intervals  $\delta t$  in each analysis interval  $\Delta t$  for which total particle counts rate  $N$  is nonzero. We then estimate  $f_Q$  from  $f_D$  by calculating the expected rate of false negatives for particle arrivals occurring as a Poisson counting process. We detail this procedure below.

By Bayes Theorem, we have:

$$f_{D|Q} = \frac{f_D f_{Q|D}}{f_Q}, \quad (\text{S1})$$

where  $f_{D|Q}$  is the conditional probability of detecting transport when it is active, and  $f_{Q|D}$  is the probability that transport is actually active when it has been detected. We observed that the Wenglor optical particle counters did not produce “false positives,” i.e. that detection necessarily implied transport and therefore that  $f_{Q|D} = 1$ . However, we found that during conditions of weak transport or few Wenglor counters, false negatives could occur with some regularity due to the limited sampling volume of individual counters. Denoting these false negatives as  $f_{\sim D|Q}$  and noting that  $f_{\sim D|Q} + f_{D|Q} = 1$ , we can restate Eq. S1 as:

$$f_Q = \frac{f_D}{1 - f_{\sim D|Q}}. \quad (\text{S2})$$

To estimate the rate of false negatives  $f_{\sim D|Q}$ , we treat particle arrivals as a Poisson counting process. For such a process:

$$f_{\sim D|Q} = \exp(-\lambda), \quad (\text{S3})$$

where  $\lambda$  is the average arrival rate of particles per  $\delta t$  averaging interval at times when transport is active. We calculate  $\lambda$  as:

$$\lambda = \bar{N} \delta t / f_D, \quad (\text{S4})$$

where  $\bar{N}$  is the mean particle counts rate during the analysis interval  $\Delta t = 1$  minute. Combining Eqs. S2-S4, we have:

$$f_Q = \frac{f_D}{1 - \exp(-\lambda)} = \frac{f_D}{1 - \exp(-\bar{N} \delta t / f_D)}. \quad (\text{S5})$$

The effect of the false negative correction in computing  $f_Q$  can be seen in Fig. S2. During strong transport,  $\lambda$  is large so  $f_Q \approx f_D$  in Eq. S5. However, when transport is weak,  $\delta t$  is small, or the number of Wenglors are few,  $\lambda$  can be much smaller than 1, and therefore the correction causes  $f_Q$  to significantly exceed  $f_D$ .

## Text S2. Estimation of uncertainties for effective threshold wind speeds, shear velocities, and shear stresses

To facilitate uncertainty estimation for computed effective thresholds, we combined effective threshold wind speed values  $u_{th}$  from individual  $\Delta t$  analysis intervals into bins defined by ranges of flux activity  $f_Q$ . For each bin, we computed bin-averaged threshold and activity values for  $u_{th}$  and  $f_Q$ , then we calculated their uncertainties from the standard errors of values in each bin.

When converting each bin-averaged effective threshold wind speed  $u_{th}$  to an effective threshold shear velocity  $u_{*,th}$  and shear stress  $\tau_{th}$ , we performed error propagation to estimate uncertainties in  $u_{*,th}$  and  $\tau_{th}$ .

### S2.1. Creation of flux activity bins

For each site, we grouped values of  $u_{th}$  for individual  $\Delta t$  together into bins covering ranges of  $f_Q$ . To accommodate the uneven spread of data points across the range of possible  $f_Q$ , we allowed for creation of bins covering varying ranges of  $f_Q$ . These criteria were established to balance the need for a sufficient number of data points in each bin with the need to limit the maximum width of the bins. The procedure for generating the binned values for each site is as follows:

- (1) Sort all  $u_{th}$  data points in order of increasing  $f_Q$ . Because the effective threshold calculation (Eq. 2) assumes intermittent transport conditions, exclude data points with  $f_Q < 0.05$  and  $f_Q > 0.95$ .
- (2) Starting from the lowest remaining  $f_Q$ , add data points to the bin, until the following criteria are achieved for the bin
  - a.  $\max(f_Q) - \min(f_Q) \geq 0.1$  (minimum bin width), AND
  - b. There are at least 3 points in the bin OR  $\max(f_Q) - \min(f_Q) > 0.2$  (maximum bin width).
- (3) Once the bin is full, repeat step 2 for the next bin.

### S2.2. Determination of mean values and uncertainties for each flux activity bin

For each bin  $i$ , we determined the mean value for flux activity  $f_{Q,i}$  and its uncertainty  $\sigma_{f_{Q,i}}$  as:

$$f_{Q,i} = \sum_j f_{Q,j} / N_i, \quad (S6)$$

$$\sigma_{f_{Q,i}} = \frac{\sqrt{\sum_j (f_{Q,j} - f_{Q,i})^2}}{\sqrt{N_i}}, \quad (S7)$$

where  $f_{Q,j}$  are the individual values of flux activity in the bin and  $N_i$  is the total number of values in the bin. Eq. S7 was computed based on the typical formulation for the standard error [Eq. 4.14 in *Bevington and Robinson, 2003*]. Similarly, the mean effective threshold wind speed  $u_{th,i}$  and its uncertainty  $\sigma_{u_{th,i}}$  are:

$$u_{th,i} = \sum_j u_{th,j} / N_i, \quad (S8)$$

$$\sigma_{u_{th,i}} = \frac{\sqrt{\sum_j (u_{th,j} - u_{th,i})^2}}{\sqrt{N_i}}, \quad (S9)$$

where  $u_{th,j}$  are the individual values of effective threshold in the bin.

### S2.3. Estimation of uncertainties for effective threshold shear velocity and shear stress

We converted binned values for effective threshold wind speed  $u_{th,i}$  to effective threshold shear velocity  $u_{*,th}$  by Eq. 3 and to effective threshold stress  $\tau_{th}$  by Eq. 4. We calculated aerodynamic roughness heights  $z_0$  in Eq. 3 for each site based on wind velocity profiles for zero transport, and we assumed the standard von Karman parameter  $\kappa \approx 0.4$ . In Supporting Information Text S3 below, we justify the use of constant values for  $z_0$  and  $\kappa$ , despite the known tendencies of these values to change systematically with saltation flux. In Eq. 4, we set the air density  $\rho_f$  based on the mean temperature at each site [Martin and Kok, 2017].

Using the error propagation formula [Eq. 3.14 in Bevington and Robinson, 2003], we propagated effective threshold wind speed uncertainty  $\sigma_{u_{th}}$  and roughness height uncertainty  $\sigma_{z_0}$  (calculated in Supporting Information Text S3 below) to derive uncertainty in threshold shear velocity  $\sigma_{u_{*,th}}$  and threshold stress  $\sigma_{\tau_{th}}$ :

$$\sigma_{u_{*,th}} = \frac{u_{*,th}}{u_{th}} \sqrt{\sigma_{u_{th}}^2 + \frac{\ln^2(\sigma_{z_0})}{\ln^2(z_U/z_0)} u_{*,th}^2}, \quad (S10)$$

$$\sigma_{\tau_{th}} = 2\rho_f u_{*,th} \sigma_{u_{*,th}}. \quad (S11)$$

### Text S3. Determination of aerodynamic roughness height and its sensitivity to variation in saltation activity

Here, we describe methods for determining aerodynamic roughness height  $z_0$ . Then we evaluate the possibility of systematic variation in saltation-influenced effective roughness height  $z_s$  with transport activity  $f_Q$ . To evaluate sensitivity of saltation-influenced von Karman parameter  $\kappa_s$  to  $f_Q$ , we assume that such von Karman sensitivity will be reflected in the sensitivity of  $z_s$ .

#### S3.1. Estimation of aerodynamic roughness height $z_0$

Under neutrally stable conditions with negligible saltation, the aerodynamic roughness height  $z_0$  describes the zero-intercept height of a linear fit to the vertical profile of horizontal wind versus the logarithm of wind height. In practice, we found that wind profile fits to calculate  $z_0$  showed large variability due to deviations from expected logarithmic law-of-the-wall profiles resulting from convective instability during periods of non-saltation (see Fig. S3 in *Martin and Kok* [2017]).

To avoid the problem of unstable profiles, we instead considered the trend in effective roughness height  $z_s$ , which is influenced both by aerodynamic conditions and by saltation-induced roughness [Sherman, 1992], versus total saltation flux  $Q$ . (Methods for estimating  $Q$  are described in *Martin and Kok* [2017] and *Martin et al.* [2017].) For successive 30-minute intervals, we estimated  $z_s$  by manipulating the law-of-the-wall:

$$z_s = z_U \exp\left(-\frac{\kappa \bar{u}}{u_{*,Re}}\right), \quad (\text{S12})$$

where  $\bar{u}$  is the mean wind speed for anemometer height  $z_U$  during the 30-minute interval,  $\kappa = 0.4$  is the von Karman parameter, and  $u_{*,Re}$  is the shear velocity determined from the Reynolds stress method [*Martin and Kok*, 2017]. We calculated  $z_s$  by Eq. S12 over 30-minute intervals, instead of the  $\Delta t = 1$  minute analysis intervals applied elsewhere in this paper, because  $u_{*,Re}$  is ill-defined at a time scale of 1 minute [*van Boxel et al.*, 2004].

Fig. S3 shows the variation in  $z_s$  with  $Q$  for each site. The logarithm of  $z_s$  increases linearly with  $Q$  up to  $Q \approx 30 \text{ gm}^{-1}\text{s}^{-1}$ . Performing a linear fit to  $\ln(z_s)$  versus  $Q$  over this range, we estimate  $z_0$  as the zero-intercept value of this fit, yielding values of  $0.707 \times 10^{-4} \text{ m}$ ,  $1.420 \times 10^{-4} \text{ m}$ , and  $0.993 \times 10^{-4} \text{ m}$ , for Jericoacoara, Rancho Guadalupe, and Oceano, respectively. Associated uncertainties in log-space, i.e.  $\sigma_{\ln(z_0)}$ , are 0.115, 0.137, and 0.128, for Jericoacoara, Rancho Guadalupe, and Oceano, respectively.

#### S3.2. Sensitivity of effective roughness height $z_s$ to changes in saltation activity $f_Q$

Values of  $z_0$  as determined above were used for conversion of threshold wind speed  $u_{th}$  to threshold shear velocity  $u_{*,th}$  and shear stress  $\tau_{th}$  as described in Eqs. 3 and 4. However, such use of  $z_0$  for this conversion may have failed to account for an increase in the effective roughness height  $z_s$  with saltation intensity, thereby leading to an underestimation of  $u_{*,th}$  in comparison to actual values.

To evaluate whether variation in  $z_s$  could have influenced our results, we directly compared measured values of  $z_s$  to  $f_Q$  over 30-minute intervals. Such comparison was only possible at Oceano, where 30-minute values of  $f_Q$  covered the full range of activities from 0 to 1. The result

of this comparison is shown in Fig. S4. Notably, there appears to be a negligible variation in  $z_s$  with  $f_Q$ . We confirm this lack of trend by performing a linear fit to  $\ln(z_s)$  versus  $f_Q$ . The best fit for this slope,  $-0.339 \pm 0.174$ , indicates a weak negative trend. Though such a result seems at odds with the obvious increase in  $z_s$  with  $Q$  (Fig. S3), we note that most intermittent transport, i.e.,  $0.05 < f_Q < 0.95$ , corresponds to relatively small saltation fluxes, for which the deviation of  $z_s$  away from  $z_0$  is negligible. We therefore assume that  $z_0$  remains constant when converting from threshold wind speeds to threshold shear velocities and shear stresses.

### S3.3. Sensitivity of effective von Karman parameter $\kappa_s$ to changes in saltation activity $f_Q$

We did not directly evaluate sensitivity of  $\kappa_s$  to  $f_Q$ . Instead, we note that  $\kappa_s$  and  $z_s$  should display similar sensitivities to  $f_Q$ . Therefore, the lack of a strong trend in  $z_s$  with  $f_Q$  suggests the lack of a trend in  $\kappa_s$  with  $f_Q$ .

## Text S4. Calculation of fluid and impact threshold stresses and shear velocities

To calculate fluid and impact threshold stresses,  $\tau_{ft}$  and  $\tau_{it}$ , at each field site, we performed linear fits to  $\tau_{th}$  versus  $f_Q$  according to Eq. 1. Here, we detail the fitting procedure to obtain  $\tau_{ft}$ ,  $\tau_{it}$ , and the uncertainty for these values. Then, we describe the calculation of the threshold shear velocity ratio and its uncertainty.

### S4.1. Calculation of fluid and impact thresholds by linear fit to saltation activity versus effective threshold stress

Following Eqs. 6.12, 6.21, 6.22, and 7.23 in *Bevington and Robinson* [2003], we performed a linear fit to  $\tau_{th}$  versus  $f_Q$ , i.e.,

$$\tau_{th} = a + b f_Q, \quad (\text{S13})$$

where  $a$  is the fitting intercept and  $b$  is the fitting slope;  $\sigma_a$ ,  $\sigma_b$ , and  $\sigma_{ab}^2$  are their respective uncertainties and covariance.

Based on the linear fit (Eq. S13), fluid and impact thresholds were calculated for each site from the best fit values corresponding respectively to  $f_Q = 0$  and  $f_Q = 1$ , i.e.:

$$\tau_{ft} = a, \quad (\text{S14})$$

$$\tau_{it} = a + b. \quad (\text{S15})$$

Corresponding uncertainties in these values were then computed as:

$$\sigma_{\tau_{ft}} = \sigma_a, \quad (\text{S16})$$

$$\sigma_{\tau_{it}} = \sqrt{\sigma_a^2 + \sigma_b^2 + 2\sigma_{ab}^2}. \quad (\text{S17})$$

### S4.2. Calculation of impact/fluid threshold shear velocity ratio and its uncertainty

The ratio of impact and fluid threshold shear velocities and the uncertainty of this ratio were calculated from  $\tau_{ft}$ ,  $\tau_{it}$ ,  $\sigma_{\tau_{ft}}$ , and  $\sigma_{\tau_{it}}$  by error propagation [Eq. 3.14 in *Bevington and Robinson*, 2003] as:

$$\frac{u_{*it}}{u_{*ft}} = \sqrt{\frac{\tau_{it}}{\tau_{ft}}}, \quad (\text{S18})$$

$$\sigma_{u_{*it}/u_{*ft}} = \frac{1}{2} \sqrt{\frac{\sigma_{\tau_{it}}^2}{\tau_{it}\tau_{ft}} + \frac{\sigma_{\tau_{ft}}^2 \tau_{it}}{\sigma_{\tau_{ft}}^3}}. \quad (\text{S19})$$

## Text S5. Selection and justification of averaging and analysis time intervals for calculations of saltation activity and effective threshold

Recognizing that calculations of saltation activity  $f_Q$  and effective threshold wind speed  $u_{th}$  are sensitive to averaging interval  $\delta t$  and analysis interval  $\Delta t$  [Stout, 1998; Barchyn and Hugenholz, 2011], here we provide physical explanations for our selection of these values. Then, we describe analyses to investigate the sensitivity of our results to the choice of these time scales.

### S5.1. Physical basis for selecting averaging and analysis intervals

Noting the possible sensitivity of  $u_{th}$  calculations to selection of  $\delta t$  and  $\Delta t$ , we chose these averaging and analysis timescales through consideration of saltation transport mechanics and the requirements of the statistical analysis. For averaging interval, we chose  $\delta t = 2\text{s}$  to match the typical 1-4 second response time of saltation to turbulent wind fluctuations [e.g., Anderson and Haff, 1988; McEwan and Willetts, 1991; Ma and Zheng, 2011]. We found that this selection of  $\delta t$  produced a general agreement between the expected threshold ratio  $u_{*,it}/u_{*,ft} = 0.82$  [Bagnold, 1937; Kok, 2010a] and observed values (Table S1). Though this selection of  $\delta t$  is somewhat arbitrary, we show below in S5.2 that changing  $\delta t$  does not qualitatively affect the outcome of our analysis.

For the analysis interval  $\Delta t$ , we require a timescale that is much larger than seconds, because of the decoupling of spatially-separated wind and saltation time series over such short timescales [e.g., Baas, 2008]. Because the typical oscillation of large-scale structures in an atmospheric boundary layer is roughly 1 minute [e.g., Guala *et al.*, 2011],  $\Phi_u$  and  $f_Q$  determined at or above this timescale should provide representative statistical snapshots of wind and saltation fluctuations. Therefore, we chose  $\Delta t = 1$  minute to satisfy these statistical sampling requirements while maximizing the number of analysis windows. Making  $\Delta t$  much larger than 1 minute would have eliminated our ability to evaluate the full range of saltation activities at Jericoacoara and Rancho Guadalupe.

### S5.2. Sensitivity analysis for effect of averaging interval

To examine the effect of averaging interval  $\delta t$  on the relation between  $f_Q$  and  $u_{th}$ , we redid the analysis from Fig. 3a for five values of  $\delta t$ : 1 s, 1.4 s, 2 s, 3 s, and 4 s. The resulting plots for Oceano, where the data are most voluminous, are shown in Fig. S5. The computed limiting values of fluid threshold  $\tau_{ft}$ , impact threshold  $\tau_{it}$ , and threshold ratio  $u_{*,it}/u_{*,ft}$ , are provided in Table S2.

There are two effects of averaging interval  $\delta t$ . First, the probability of detecting particles in each averaging interval increases with  $\delta t$ . This “flux detection effect” increases  $f_Q$  with increasing  $\delta t$ , and therefore it decreases  $u_{th}$  by Eq. 2. Second, by averaging over extreme events, the distribution of wind speeds  $\Phi_u$  narrows with increasing  $\delta t$ . For small  $f_Q$ , this “wind distribution effect” will decrease  $u_{th}$  with increasing  $\delta t$ ; for large  $f_Q$ , it will increase  $u_{th}$  with increasing  $\delta t$ .

The outcome of these two effects can be seen in Fig. S5. The fluid threshold  $\tau_{ft}$ , which corresponds to the lower limit  $f_Q \rightarrow 0$ , displays a substantial decrease in  $\tau_{th}$  with increasing  $\delta t$  by a combination of the flux detection effect and the wind distribution effect. In contrast, the impact threshold  $\tau_{it}$ , which corresponds to the upper limit  $f_Q \rightarrow 1$ , shows a minor increase in  $\tau_{th}$

with increasing  $\delta t$ , as the increase from the wind distribution effect slightly outweighs the decrease by the flux detection effect. The combined result of decreasing  $\tau_{ft}$  and increasing  $\tau_{it}$  is to increase the threshold ratio  $u_{*,it}/u_{*,ft}$  with increasing  $\delta t$  (Table S2).

### S5.3. Sensitivity analysis for effect of analysis interval

At Oceano, where the data are significantly more extensive than at the other sites, we were able to perform a sensitivity analysis to evaluate the effect of varying the analysis interval from 0.5 to 10 minutes. Holding averaging interval  $\delta t$  constant at 2 s, we considered 5 values for  $\Delta t$  at Oceano: 0.5 minutes, 1 minute, 2 minutes, 5 minutes, and 10 minutes. The resulting calculations of  $\tau_{th}$  versus  $f_Q$  are shown in Fig. S6. The computed limiting values of fluid threshold  $\tau_{ft}$ , impact threshold  $\tau_{it}$ , and threshold ratio  $u_{*,it}/u_{*,ft}$ , are provided in Table S3. In all cases, the effect of changing  $\Delta t$  is negligible.

## Text S6. Sensitivity of results to atmospheric and surface trends

In this section, we describe sensitivity analyses to indirectly consider the effects of variability of atmospheric and surface conditions on the determination of effective thresholds and limiting fluid and impact threshold values. For these sensitivity analyses, we sorted the data from Oceano in two ways: (1) by time of day, and (2) by date. Separating data by time of day was meant to capture diurnal variations in atmospheric and surface properties, such as atmospheric stability, humidity, and soil moisture. Separating data by date was meant to capture secular variations in grain size and sorting properties, as surface grain size tended to coarsen over time at Oceano.

### S6.1. Sensitivity analysis by time of day

We separated the data into three components of the diurnal cycle that constituted most measured saltation flux at Oceano: 12-14h, 14-16h, and 16-18h. The resulting variation of effective threshold  $\tau_{th}$  with transport activity  $f_Q$  is shown in Fig. S7, and corresponding limiting impact and fluid threshold values are given in Table S4. Though the three diurnal periods do show some variation in limiting fluid and impact threshold values, there is no systematic trend of increasing or decreasing thresholds through the course of the day. Furthermore, the separation between fluid and impact threshold is maintained throughout the day.

### S6.2. Sensitivity analysis by date

We separated the data into three ranges of dates for which saltation flux was measured at Oceano: May 15-19, May 23-28, and June 1-4, 2015. The resulting variation of effective threshold  $\tau_{th}$  with transport activity  $f_Q$  is shown in Fig. S8, and corresponding limiting impact and fluid threshold values are given in Table S5. Notably,  $\tau_{it}$  for the May 23-28 and June 1-4 periods does appear to be larger than for May 15-19. This increase in the threshold corresponds to a slight coarsening of median grain diameter during these later periods (Table S5). This supports the notion that thresholds increase with grain diameter. In all cases, the trend of effective threshold  $\tau_{th}$  decreasing with transport activity  $f_Q$  is maintained.

## Text S7. List of variables

Below, we list all variables described in the manuscript. Typical units for variables are given in parentheses, if applicable.

### S7.1. Variables in main text

$\tau$  = wind shear stress (Pa)  
 $\tau_{ft}$  = fluid threshold shear stress (Pa)  
 $\tau_{it}$  = impact threshold shear stress (Pa)  
 $\tau_{th}$  = effective threshold shear stress (Pa)  
 $u_*$  = shear velocity (m/s)  
 $u_{*ft}$  = fluid threshold shear velocity (m/s)  
 $u_{*it}$  = impact threshold shear velocity (m/s)  
 $u_{*it}/u_{*ft}$  = shear velocity threshold ratio  
 $u_{*,th}$  = effective threshold shear velocity (m/s)  
 $u(t)$  = time series of horizontal wind speed (m/s)  
 $u_{ft}$  = fluid threshold wind speed (m/s)  
 $u_{it}$  = impact threshold wind speed (m/s)  
 $u_{th}$  = effective threshold wind speed (m/s)  
 $f_Q$  = saltation transport activity  
 $\Phi_u$  = cumulative distribution of streamwise wind speed  $u$   
 $N$  = vertically integrated saltation particle counts rate (counts/s)  
 $z_U$  = anemometer height above the sand surface (m)  
 $\delta t$  = averaging time interval (s)  
 $\Delta t$  = analysis time interval (minutes)  
 $\kappa$  = von Karman parameter  
 $z_0$  = aerodynamic roughness height (m)  
 $z_s$  = effective roughness height, accounting for saltation-induced roughness (m)  
 $\rho_f$  = air density (kg/m<sup>3</sup>)  
 $z/L$  = stability parameter  
 $\theta$  = angle of horizontal wind relative to dominant sand-transporting wind  
 $Q$  = saltation flux (g/m/s)  
 $\tau_0$  = bed surface shear stress (Pa)  
 $\tau_{th,flux}$  = flux-based estimate of threshold stress (Pa)

### S7.2. Additional variables in Supporting Information

$f_D$  = saltation detection rate  
 $f_{Q|D}$  = probability that transport is actually active when it has been detected  
 $f_{D|Q}$  = conditional probability of detecting transport when it is active  
 $f_{\sim D|Q}$  = conditional probability of not detecting transport when it is active  
 $\lambda$  = average arrival rate of particles (counts/s)  
 $\bar{N}$  = mean vertically integrated saltation particle counts rate (counts/s)  
 $f_{Q,i}$  = mean value for saltation transport activity for bin  $i$   
 $\sigma_{f_{Q,i}}$  = uncertainty in saltation transport activity for bin  $i$   
 $f_{Q,j}$  = individual values  $j$  of saltation activity in bin  $i$

$N_i$  = number of values in bin  $i$

$u_{th,i}$  = mean value for effective threshold wind speed for bin  $i$  (m/s)

$\sigma_{u_{th,i}}$  = uncertainty in effective threshold wind speed for bin  $i$  (m/s)

$u_{th,j}$  = individual values  $j$  of effective threshold wind speed in bin  $i$  (m/s)

$\sigma_{u_{*,th}}$  = uncertainty in effective threshold shear velocity (m/s)

$\sigma_{\tau_{th}}$  = uncertainty in effective threshold shear stress (Pa)

$\bar{u}$  = 30-minute mean wind speed (m/s)

$\sigma_{\ln(z_0)}$  = natural log uncertainty in aerodynamic roughness height

$\kappa_s$  = effective von Karman parameter, accounting for saltation effects

$a$  = least squares linear fitting intercept

$\sigma_a$  = uncertainty in fitting intercept

$b$  = least squares linear fitting slope

$\sigma_b$  = uncertainty in fitting slope

$\sigma_{ab}^2$  = covariance of fitting slope and intercept

$\sigma_{\tau_{ft}}$  = uncertainty in fluid threshold stress (Pa)

$\sigma_{\tau_{it}}$  = uncertainty in impact threshold stress (Pa)

$\sigma_{u_{*it}/u_{*ft}}$  = uncertainty in shear velocity threshold ratio

$d_{50}$ , median diameter of surface particles by volume (mm)

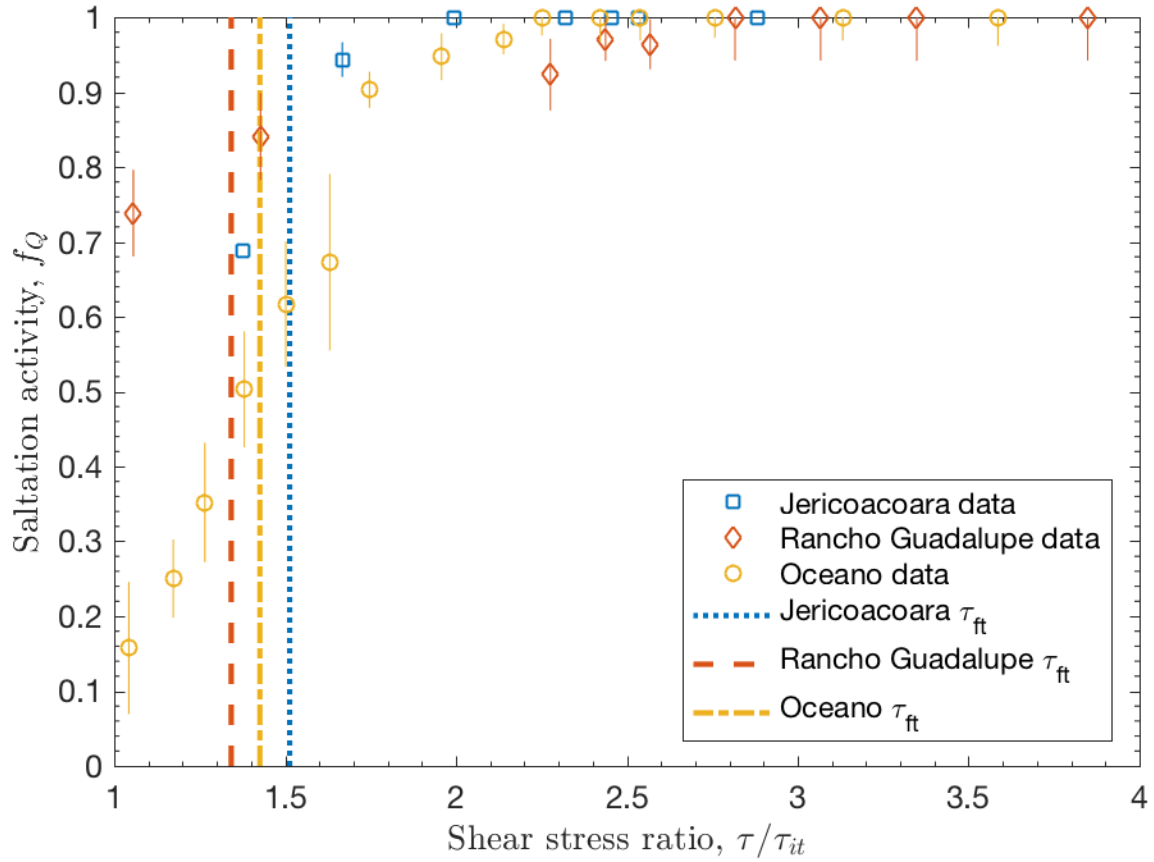


**Figure S1.** Saltation transport activity  $f_Q$  versus Reynolds shear stress ratio  $\tau/\tau_{it}$ . Values are computed over 30-minute intervals and combined into bins by range of  $\tau$ . Error bars indicate standard error for each bin. Dashed lines indicate fluid threshold  $\tau_{ft}$  at each site from Fig. 3.

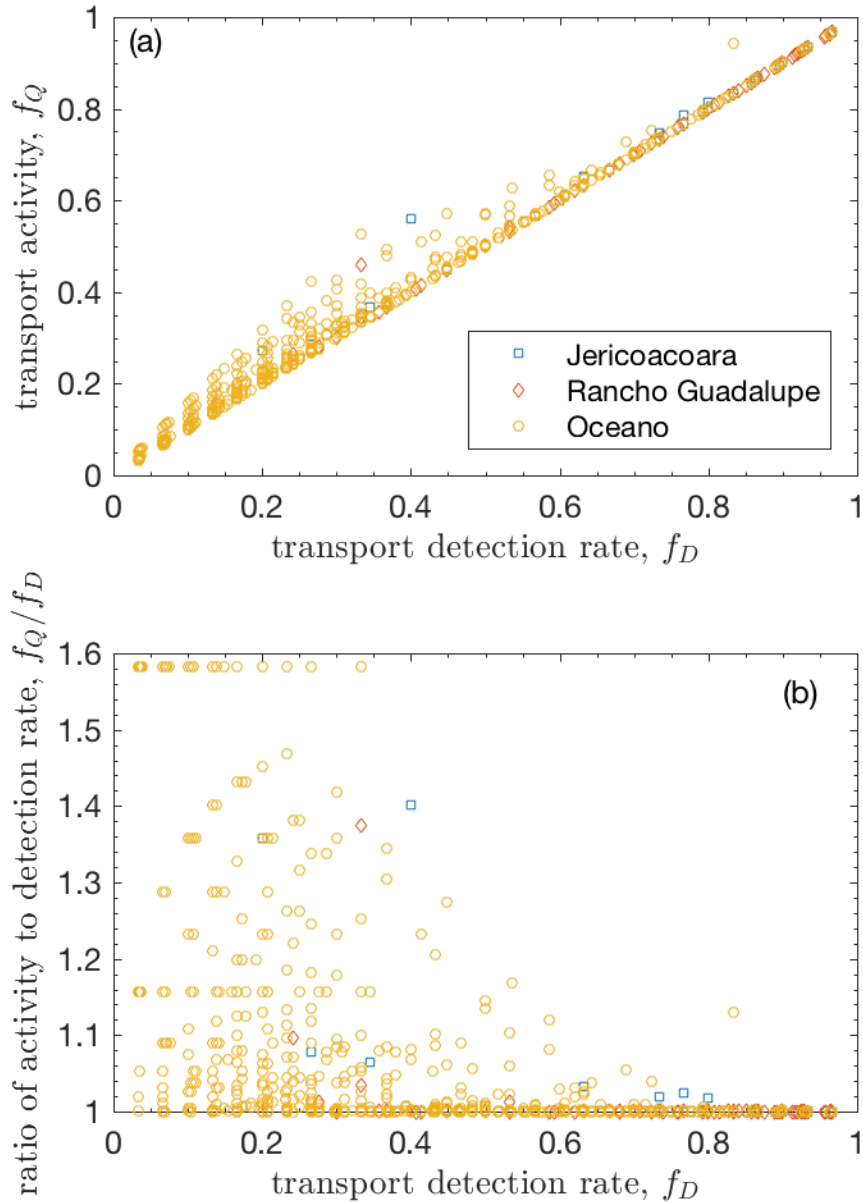


**Figure S2.** (a) Comparison of saltation transport activity  $f_Q$ , which includes correction for estimated rate of false negatives (Eq. S5), to the actual transport detection rate  $f_D$ . (b) Ratio of transport activity to detection rate  $f_Q/f_D$  versus detection rate  $f_D$ , illustrating the relative magnitude of the correction for false negatives. This correction tends to be strongest when transport is weak, due to the higher probability of false negatives. The difference between  $f_Q$  and  $f_D$  is also affected by changes in the background particle detection rate, which can be affected by the number and height of Wenglor detectors and the nature of transport fluctuations.

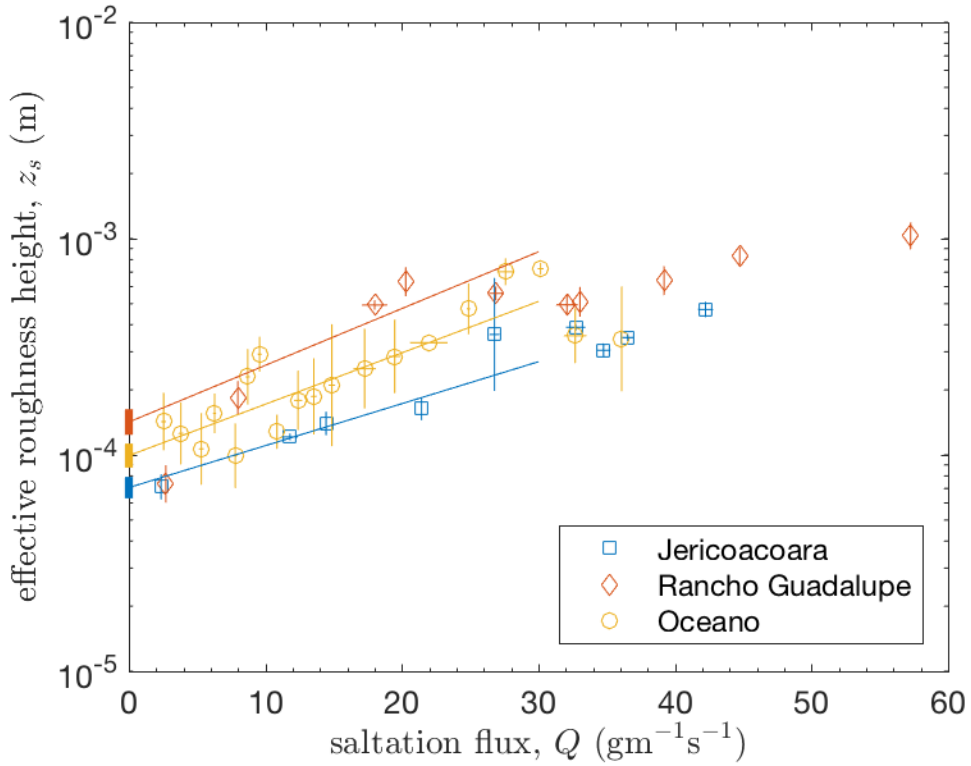


**Figure S3.** Comparison of effective roughness height  $z_s$  versus total saltation flux  $Q$  at each field site. We estimate  $z_0$  as the zero-intercept of the linear fit of  $\ln(z_s)$  versus  $Q$  at each site for  $Q \leq 30 \text{ gm}^{-1}\text{s}^{-1}$ , indicated by the thin lines. Resulting calculated  $z_0$  values for each site are shown as thick vertical bars at  $Q = 0 \text{ gm}^{-1}\text{s}^{-1}$ . The vertical range of these bars corresponds to uncertainties in  $z_0$  as determined by the linear fits.

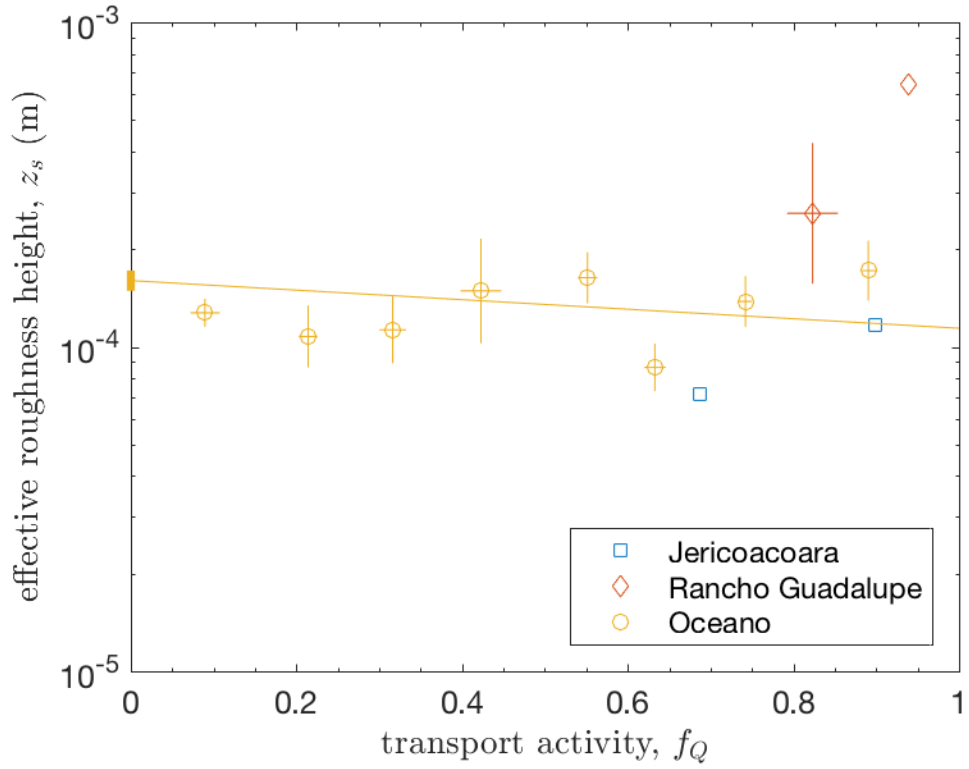


**Figure S4.** Comparison of effective roughness height  $z_s$  versus saltation transport activity  $f_Q$  for intermittent transport ( $0.05 < f_Q < 0.95$ ). Values are calculated over 30-minute intervals and combined into bins by  $f_Q$ . Ranges of 30-minute  $f_Q$  values at Jericoacoara and Rancho Guadalupe were insufficient for binning and fitting.

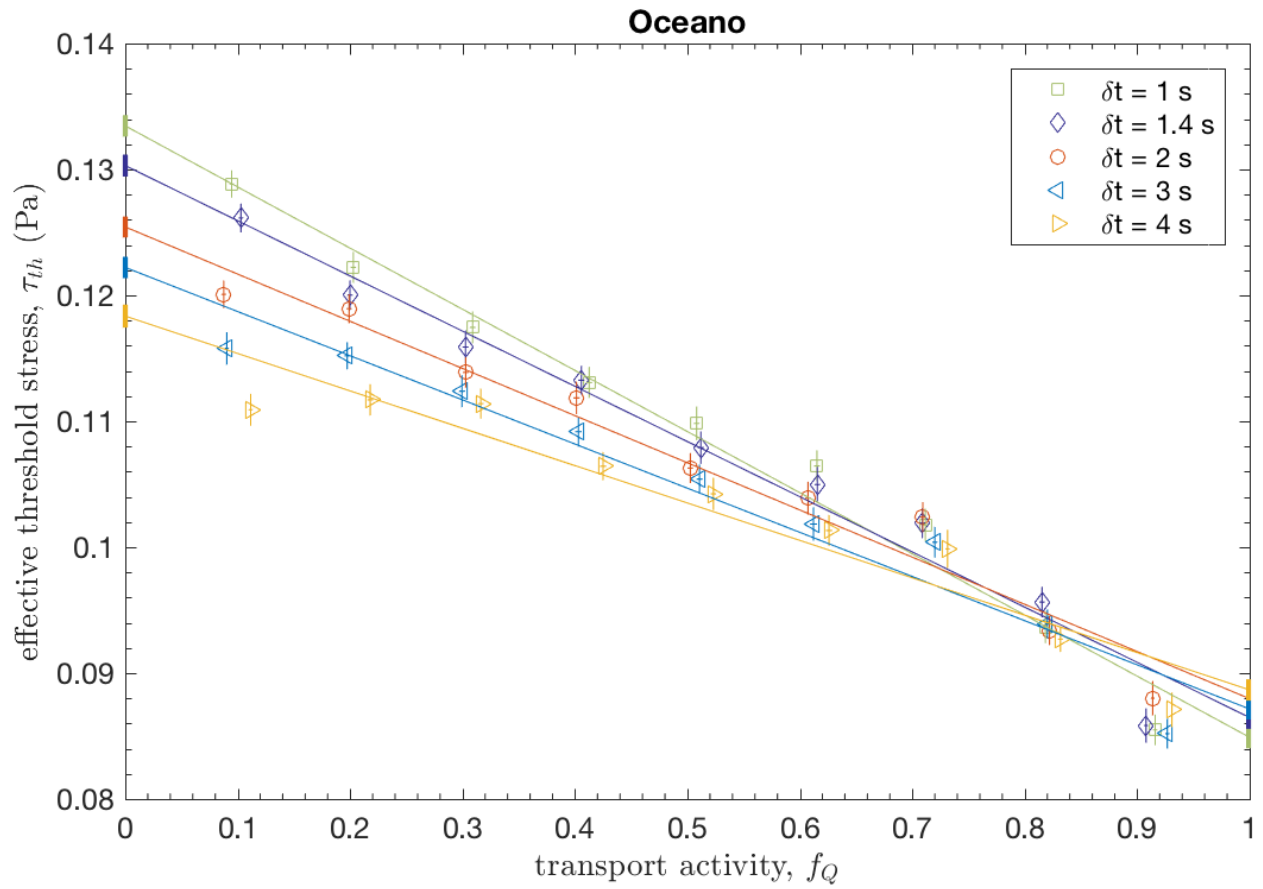


**Figure S5.** Comparison of effective threshold  $\tau_{th}$  and saltation transport activity  $f_Q$  for five averaging intervals  $\delta t$  at Oceano. Analysis interval  $\Delta t$  was fixed at 1 minute for this analysis. Limiting fluid and impact threshold values, indicated by vertical bars at  $f_Q = 0$  and  $f_Q = 1$ , respectively, are given in Table S2.

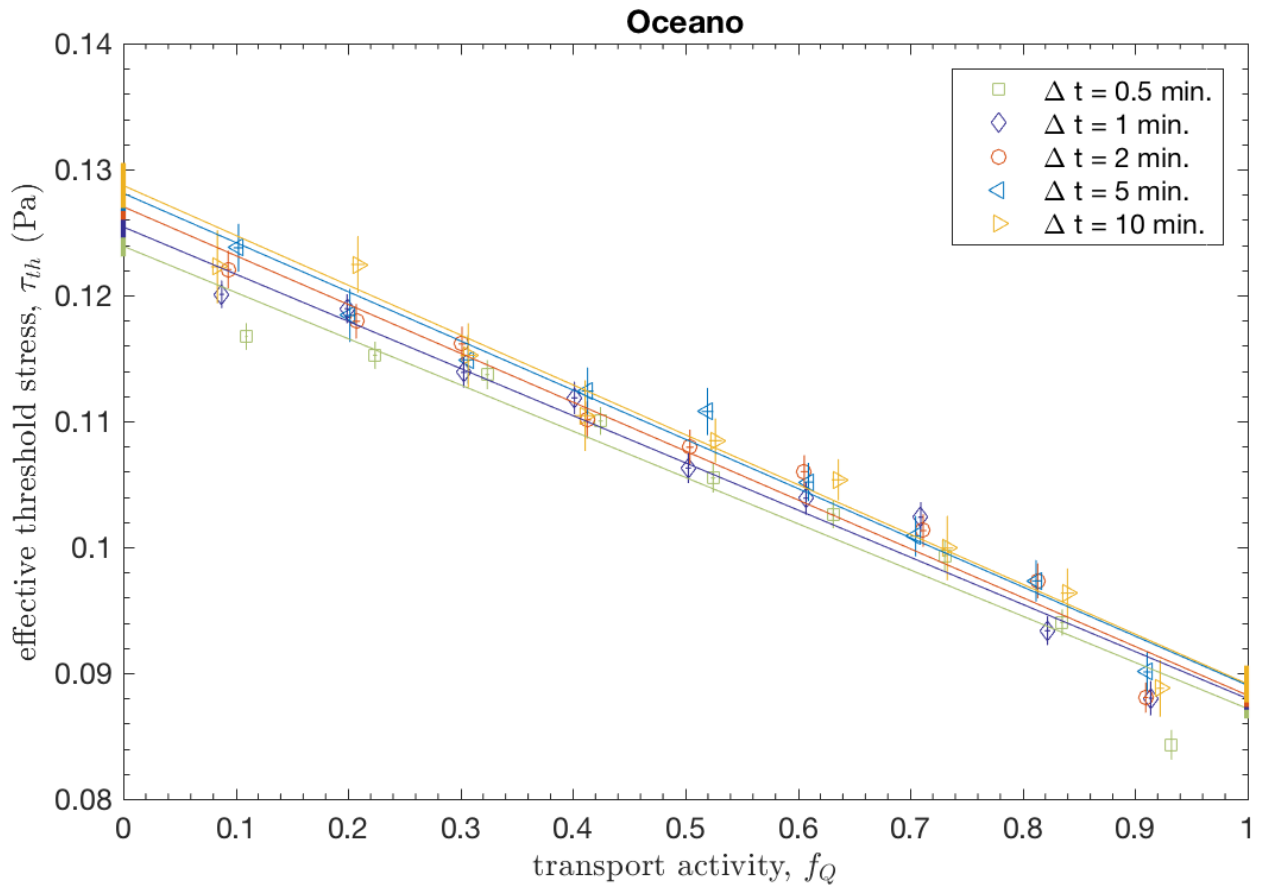


**Figure S6.** Comparison of effective threshold  $\tau_{th}$  and saltation transport activity  $f_Q$  for five different analysis intervals  $\Delta t$  at Oceano. Averaging interval  $\delta t$  was fixed at 2 s for this analysis. Limiting fluid and impact threshold values, indicated by vertical bars at  $f_Q = 0$  and  $f_Q = 1$ , respectively, are given in Table S3.

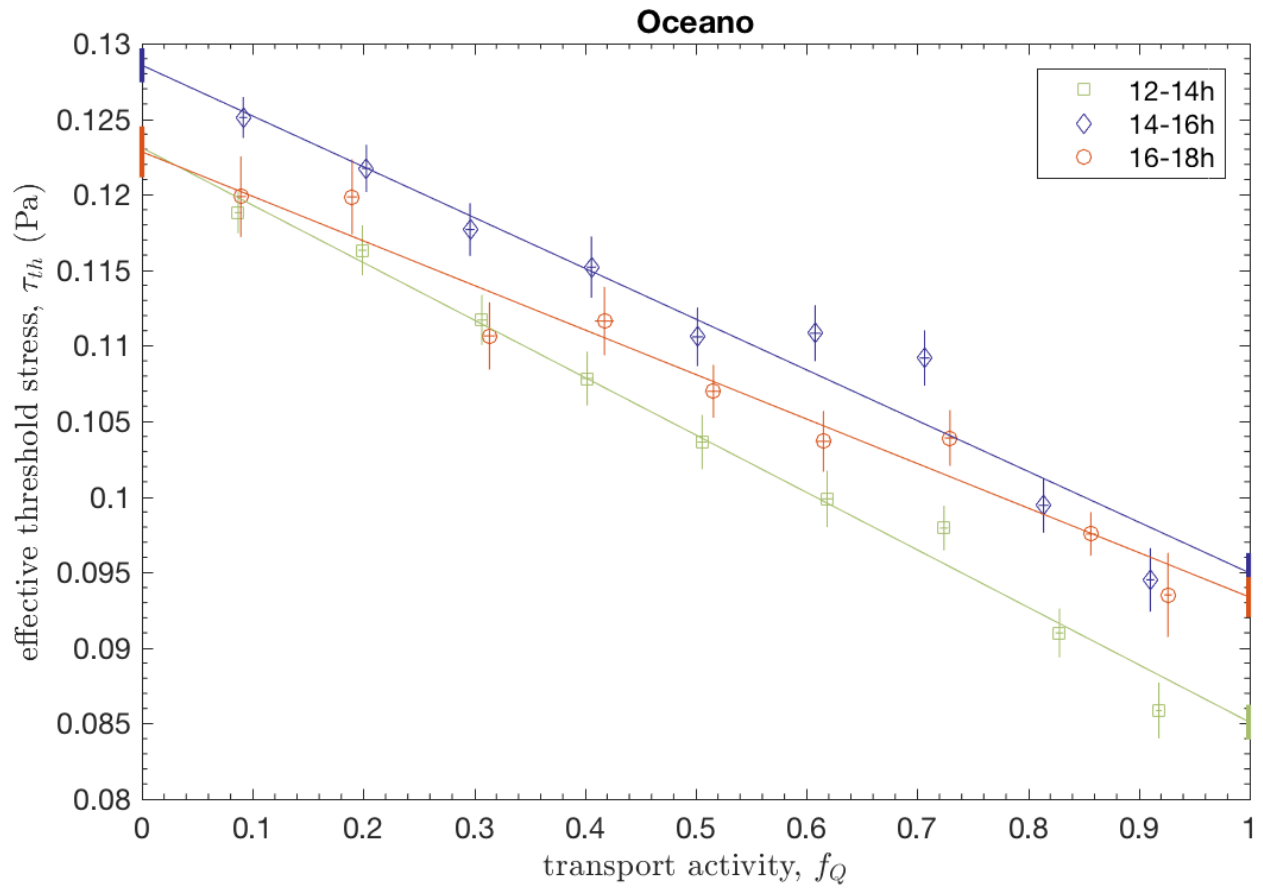


**Figure S7.** Comparison of effective threshold  $\tau_{th}$  and saltation transport activity  $f_Q$  for three different time periods for the diurnal cycle at Oceano. Limiting fluid and impact threshold values, indicated by vertical bars at  $f_Q = 0$  and  $f_Q = 1$ , respectively, are given in Table S4.

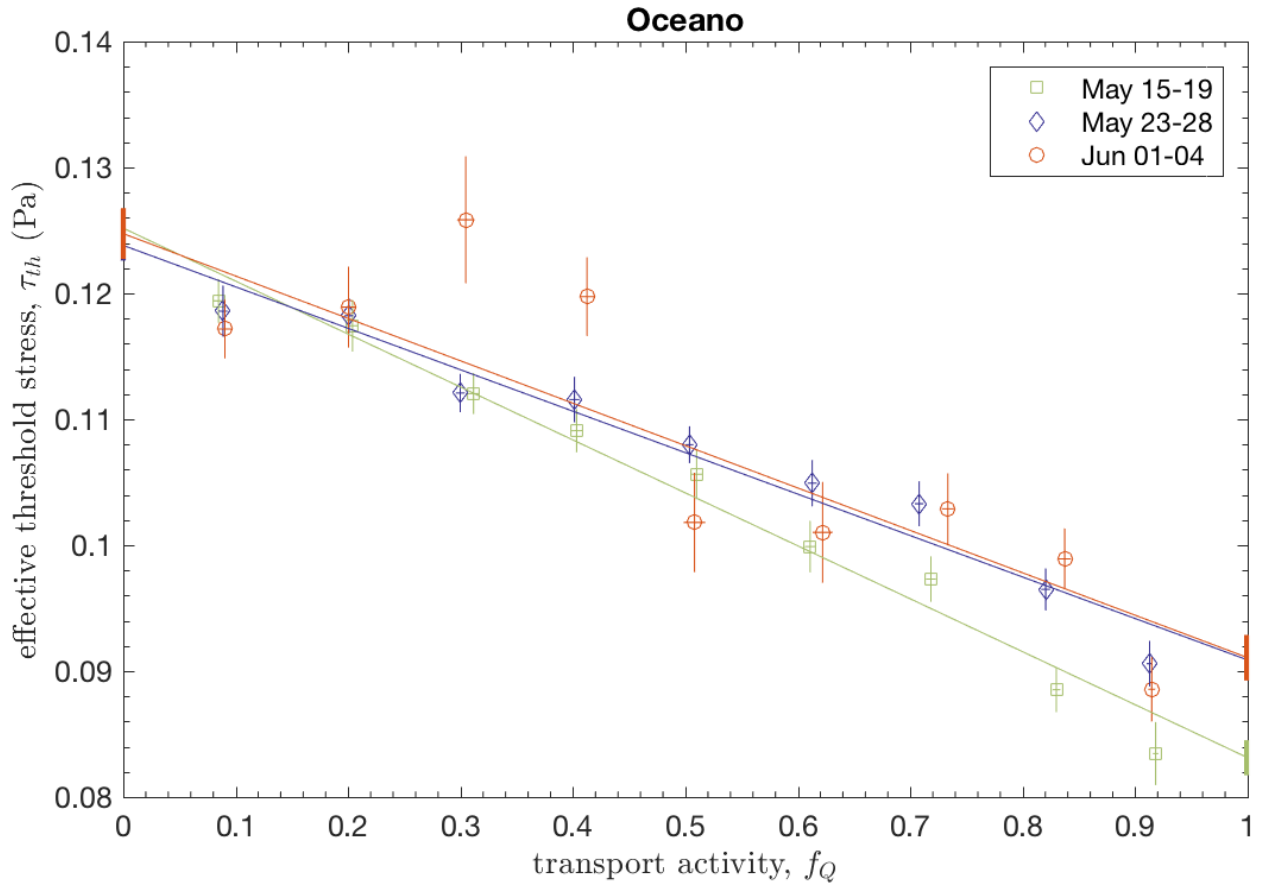


**Figure S8.** Comparison of effective threshold  $\tau_{th}$  and saltation transport activity  $f_Q$  for three segments of the deployment at Oceano, for which median surface grain diameter was respectively  $d_{50} = 0.35$  mm, 0.42 mm, and 0.42 mm. Limiting fluid and impact threshold values, indicated by vertical bars at  $f_Q = 0$  and  $f_Q = 1$ , respectively, are given in Table S5.

**Table S1.** Threshold values for primary analysis with  $\delta t = 2\text{s}$  averaging interval and  $\Delta t = 1\text{ minute}$  analysis interval. Median grain diameter of surface particles at each site is also included for reference.

Site	Median grain diameter, $d_{50}$ (mm)	Fluid threshold stress, $\tau_{ft}$ (Pa)	Impact threshold stress, $\tau_{it}$ (Pa)	Threshold ratio, $u_{*,it}/u_{*,ft}$	Threshold from flux-law fit, $\tau_{th,flux}$ (Pa)
Jericoacoara	$0.526 \pm 0.037$	$0.168 \pm 0.004$	$0.111 \pm 0.002$	$0.813 \pm 0.018$	$0.135 \pm 0.015$
Rancho Guadalupe	$0.533 \pm 0.026$	$0.147 \pm 0.006$	$0.110 \pm 0.002$	$0.863 \pm 0.027$	$0.110 \pm 0.021$
Oceano	$0.398 \pm 0.070$	$0.125 \pm 0.001$	$0.088 \pm 0.001$	$0.837 \pm 0.007$	$0.094 \pm 0.006$

**Table S2.** Best fit values for averaging interval  $\delta t$  sensitivity analysis at Oceano shown in Fig. S5. Uncertainties correspond to linear fitting uncertainty, which accounts for the uncertainty in the individual data points used for this fitting.

Averaging interval, $\delta t$ (s)	Fluid threshold, $\tau_{ft}$ (Pa)	Impact threshold, $\tau_{it}$ (Pa)	Threshold ratio, $u_{*,it}/u_{*,ft}$
1	0.133 $\pm$ 0.001	0.085 $\pm$ 0.001	0.798 $\pm$ 0.008
1.4	0.130 $\pm$ 0.001	0.086 $\pm$ 0.001	0.815 $\pm$ 0.008
2	0.125 $\pm$ 0.001	0.088 $\pm$ 0.001	0.837 $\pm$ 0.007
3	0.122 $\pm$ 0.001	0.087 $\pm$ 0.001	0.844 $\pm$ 0.007
4	0.118 $\pm$ 0.001	0.089 $\pm$ 0.001	0.866 $\pm$ 0.007

**Table S3.** Best fit values for the sensitivity analysis of the analysis interval  $\Delta t$ , shown in Fig. S6 for Oceano.

Analysis interval, $\Delta t$ (minutes)	Fluid threshold, $\tau_{ft}$ (Pa)	Impact threshold, $\tau_{it}$ (Pa)	Threshold ratio, $u_{*,it}/u_{*,ft}$
0.5	0.124 $\pm$ 0.001	0.087 $\pm$ 0.001	0.839 $\pm$ 0.007
1	0.125 $\pm$ 0.001	0.088 $\pm$ 0.001	0.837 $\pm$ 0.007
2	0.127 $\pm$ 0.001	0.088 $\pm$ 0.001	0.833 $\pm$ 0.008
5	0.128 $\pm$ 0.001	0.089 $\pm$ 0.001	0.834 $\pm$ 0.010
10	0.129 $\pm$ 0.002	0.089 $\pm$ 0.001	0.832 $\pm$ 0.013

**Table S4.** Best fit values for diurnal cycle sensitivity analysis shown in Fig. S7 for Oceano.

Diurnal time interval	Fluid threshold, $\tau_{ft}$ (Pa)	Impact threshold, $\tau_{it}$ (Pa)	Threshold ratio, $u_{*,it}/u_{*,ft}$
12-14h	$0.123 \pm 0.001$	$0.085 \pm 0.001$	$0.831 \pm 0.010$
14-16h	$0.129 \pm 0.001$	$0.095 \pm 0.001$	$0.859 \pm 0.010$
16-18h	$0.123 \pm 0.002$	$0.093 \pm 0.001$	$0.872 \pm 0.011$

**Table S5.** Best fit values for date interval sensitivity analysis shown in Fig. S8 for Oceano. Median surface grain diameters  $d_{50}$  are also provided for these date intervals.

Date interval	Median grain diameter, $d_{50}$	Fluid threshold, $\tau_{ft}$ (Pa)	Impact threshold, $\tau_{it}$ (Pa)	Threshold ratio, $u_{*,it}/u_{*,ft}$
May 15-19	$0.346 \pm 0.053$	$0.125 \pm 0.001$	$0.083 \pm 0.001$	$0.815 \pm 0.012$
May 23-28	$0.417 \pm 0.056$	$0.124 \pm 0.001$	$0.091 \pm 0.001$	$0.857 \pm 0.010$
June 1-4	$0.415 \pm 0.074$	$0.125 \pm 0.002$	$0.091 \pm 0.002$	$0.854 \pm 0.015$

## Dataset S1: Activity and threshold values

A spreadsheet containing data described in this paper may be accessed through the Zenodo data repository at <http://doi.org/10.5281/zenodo.574896>. These data are for the primary analysis presented in the main text with averaging interval  $\delta t = 2$  second for all  $\Delta t = 1$  minute analysis intervals at each field site. The spreadsheet contains the following fields:

- Date of analysis interval (“Date”).
- Start time of analysis interval (“StartTime”).
- End time of analysis interval (“EndTime”).
- Calculated transport activity  $f_Q$  (“f\_Q”).
- Calculated effective threshold wind speed  $u_{th}$  (“u\_th”) in m/s. This value is undefined (“NaN”) for intervals with  $f_Q = 0$  or  $f_Q = 1$ .
- Stability parameter  $z/L$  (“z/L”) obtained from wind-speed fluctuations in corresponding 30-minute time interval. This value is sometimes undefined (“NaN”) for intervals of very weak wind.
- Wind direction  $\theta$  (“theta”) in degrees. Value is relative to dominant wind direction at site.

The field measurements from which these values were calculated are described in *Martin et al. [2017]*.